State-dependency of dynamic and thermodynamic contributions to effective precipitation changes

Laura Braschoss[1], Nils Weitzel[1], Jean-Philippe Baudouin[1], and Kira Rehfeld[1,2]

[1] Department of Geosciences, University of Tübingen, Tübingen, Germany

[2] Department of Physics, University of Tübingen, Tübingen, Germany

Contact: Nils Weitzel (nils.weitzel@uni-tuebingen.de)

Reliable projections of the future hydrological cycle are needed for designing adaptation and mitigation measures under global warming. However, uncertainties in the projected sign and magnitude of effective precipitation changes (precipitation minus evaporation, $P - E$) remain high. Here, we examine the state-dependency of circulation, temperature, and relative humidity contributions to $P - E$ changes in simulations of the Last Glacial Maximum (LGM), mid-Holocene, and abrupt quadrupling of the atmospheric carbon dioxide concentration. To this purpose, we apply a moisture budget decomposition and a thermodynamic scaling approximation to CMIP6/PMIP4 simulations with the Earth system model MPI-ESM1.2. We find that the importance of thermodynamic and dynamic contributions to $P - E$ changes and the patterns of dynamic contributions depend strongly on the underlying forcing. Greenhouse gas forcing leads to a stronger thermodynamic than dynamic response. The LGM ice sheets yield a large dynamic contribution with zonally heterogeneous patterns. Orbital forcing induces a predominantly dynamic response with a hemispherically anti-symmetric structure. We also identify state invariant features: the importance of temperature and relative humidity contributions to specific humidity changes is consistent across states, and the wet-get-wetter-dry-get-drier paradigm proposed for global warming holds in almost all regions dominated by thermodynamic contributions. By definition, the $P - E$ budget is closed in the global mean. We find that, additionally, the respective thermodynamic, dynamic, and transient eddy contributions vanish in the global mean. Moreover for increasing length scales, the spatial variability of these contributions decays with similar rates. We suggest repeating our analysis for more models and states which could help constraining hydroclimate projections.

Significance statement: We aim at improving our understanding of the influence of changes in winds and water vapor on the local balance between precipitation and evaporation. To this end, we compare simulations for two past climate states with an idealized high carbon dioxide concentration scenario. We find characteristics that depend on the underlying state and characteristics that are consistent across states. Our results help to identify what we can learn from past climate states about precipitation changes under future greenhouse gas emission scenarios. So far, we only analyzed simulations from one model. Therefore, we suggest to repeat our analysis with more models and for more past climate states to confirm our results.

1 Introduction

Global warming induces changes in the strength and seasonality of the hydrological cycle which are evident in altered global and regional precipitation patterns (Douville et al., 2021). This leads to potentially large impacts on food security and economic prosperity through localized changes in water availability, which are controlled by the large-scale atmospheric circulation and small scale physical processes (Allan et al., 2020; Douville et al., 2021). Therefore, reliable global, regional, and local hydroclimate projections are needed to design adaptation and mitigation measures. Despite substantial improvements in resolution and complexity of state-of-the-art climate models, uncertainties on the sign and magnitude of regional moisture availability changes remain high (Douville et al., 2021). The difference between precipitation and evapotranspiration ($P - E$), also called effective precipitation, is a convenient diagnostic for changes in the local hydrological balance: it serves as a source and sink term for the atmospheric water budget and, in a quasi-equilibrium climate state, its long-term global mean is zero (Held and Soden, 2006). Over land, it modulates soil moisture and is balanced by runoff in the long-term. Additionally, it regulates sea surface salinity and is, thus, a controlling factor of the ocean overturning circulation (e.g., Armstrong et al., 2023; Jiang et al., 2021; Mehling et al., 2023).

We draw on a decomposition of the atmospheric moisture budget following Seager et al. (2010), which facilitates isolating drivers of past and projected future hydroclimate changes. Expressing $P - E$ via the moisture flux convergence, its multi-year mean changes can be separated into mean and variability (transient eddy) components. Splitting the former additionally into contributions from specific humidity changes, atmospheric circulation changes, and coupled humidity and wind changes, allows isolating thermodynamic, dynamic, and nonlinear $P - E$ changes. Using this decomposition, for example, Elbaum et al. (2022) showed that uncertainties in regional $P - E$ projections are predominantly related to inter-model differences in the dynamic component, which hints at overemphasized thermodynamic changes in the often-used multi-model mean projections.

Considering only $P - E$ changes due to the temperature-driven local increase of specific humidity (Clausius-Clapeyron relationship), Held and Soden (2006) computed a *thermodynamic scaling* of $P-E$. This scaling predicts an intensification of positive (wet) and negative (dry) $P - E$ values under global warming, termed the "wet-get-wetter-dry-get-drier" (WWDD) paradigm. The WWDD paradigm provides a good first order approximation of zonal mean $P - E$ changes under increased greenhouse gas (GHG) concentrations (Byrne and O'Gorman, 2015; Held and Soden, 2006). However, it is not effective on regional scales as shown in numerous observational and modeling studies (e.g., Chou et al., 2009; Greve et al., 2014; Polson et al., 2013; Roderick et al., 2014). In particular, multi-year mean $P - E$ over land is balanced by runoff and, therefore, by definition positive. Hence, the WWDD paradigm predicts wetting of all land areas which is not supported by observations from the last century and future projections (Douville et al., 2021; Liu and Allan, 2013).

To overcome this limitation, Byrne and O'Gorman (2015) derived an extension of the thermodynamic scaling that takes changes in horizontal temperature gradients and relative humidity into account. This scaling predicts simulated future zonal and regional annual mean $P - E$ changes substantially better (Byrne and O'Gorman, 2015; Douville et al., 2021). However, the applicability and limitations of the WWDD paradigm remain an active research area (e.g., Li et al., 2021; Yang et al., 2019; Zaitchik et al., 2023). Throughout this study, we refer to positive (negative) $P - E$ as wet (dry) and positive (negative) $P - E$ changes as wetting (drying) as a suitable dryness measure for global-scale analyses. We acknowledge that there are other dryness indicators, e.g., based on soil moisture, atmospheric water vapor deficit, or biomass productivity, which may be more suitable for different research questions (Fu and Feng, 2014; Gimeno-Sotelo et al., 2024; Li et al., 2024; Scheff et al., 2017; Vicente-Serrano et al., 2010; Řehoř et al., 2024).

The applicability of conceptual frameworks for the hydroclimate response to large climate perturbations can be tested using past climate states (e.g., Boos, 2012; D'Agostino et al., 2017; Lowry and Morrill, 2019; Rehfeld et al., 2020). The Last Glacial Maximum (LGM, $\sim 21,000$ years before present) and mid-Holocene (midH, $\sim 6,000$ years before present) are well-studied periods with strongly differing boundary conditions such as latitudinal and seasonal insolation distributions (orbital forcing), GHG concentrations, ice sheet configurations, and land-sea masks (Kageyama et al., 2018). The climate dur-

ing the LGM has gained particular interest in past-to-future comparisons: compared to pre-industrial conditions (PI, ∼1850 CE), the LGM experienced much lower CO_2 concentrations of approximately 190 ppm (Bereiter et al., 2015) and expanded (Northern Hemisphere) ice sheets, but only weak orbital forcing (Berger, 1978). This makes it a potential candidate for a cold world analog to a warmer future (Quade and Broecker, 2009). In line with the reverse analog perspective, the thermodynamic scaling of Held and Soden (2006) suggests a dry-get-wetter-wet-get-drier (DWWD) structure for the LGM. The midH is characterised by an altered seasonal and latitudinal insolation distribution due to differing orbital parameters (Otto-Bliesner et al., 2017), but small changes in GHG concentrations and ice sheet configurations compared to the PI. The orbital forcing resulted, for example, in warmer Northern Hemisphere summers, stronger boreal summer monsoons, and weaker austral summer monsoons (Brierley et al., 2020; D'Agostino et al., 2019, 2020).

The climate of the LGM is typically characterized as cold and dry. The latter is deduced particularly from a wide-spread reduction of vegetation productivity and reported evidence for more open landscapes (McGee, 2020). However, this characterization has been challenged (e.g., Lowry and Morrill, 2019; Scheff et al., 2017) and it is now largely acknowledged that effective precipitation changes followed a more nuanced regional pattern (e.g., Adam et al., 2021; Weij et al., 2024). The regionalized structure of $P - E$ changes, likely associated with the ice sheet forcing during the LGM, was also identified by Boos (2012) as the reason for a much worse performance of the thermodynamic scaling for approximating simulated $P - E$ changes compared to the future scenarios studied by Held and Soden (2006). More generally, the response of individual moisture budget contributions seems to vary substantially between regions and climate states (e.g., D'Agostino et al., 2020; Lora, 2018; Lowry and Morrill, 2019; Wills et al., 2016). This raises the question to what extent the characteristics of the different moisture budget terms depend on the spatial structure and strength of the forcing, and on state-independent properties like the geographical location. More specifically, comparing results for LGM, midH, and an idealized warm climate state resulting from an abrupt quadrupling of CO_2 (4xCO$_2$), we study the following research questions:

1. How does the spatial structure of the forcing influence the large-scale patterns and relative importance of moisture budget contributions?

2. Are the global-scale contributions and interrelationships of the moisture budget terms state-invariant?

3. Which factors control the applicability of the WWDD paradigm across states?

4. For which moisture budget contributions is the LGM a reasonable reverse analog for future hydroclimate projections?

We analyze the characteristics of the moisture budget (Sect. 3.1) and thermodynamic scaling (Sect. 3.2) components with a particular focus on the state-dependency of the patterns and relative importance of individual components, the closure and rates of decay of moisture budget contributions on large spatial scales, and the applicability of the WWDD paradigm (Sect. 4). Finally, we discuss the identified state-dependent and state-invariant features of $P - E$ changes and make suggestions for future research (Sect. 5).

2 Data

In this study, we analyze simulated changes in $P - E$ between a base climate (here given by PI conditions) and three other climate states using CMIP6/PMIP4 simulations with the MPI-ESM model version 1.2 (Mauritsen et al., 2019). CMIP and PMIP are standard experimental frameworks in (paleo)climate research, facilitating the comparability of results from different climate models (Eyring et al., 2016; Kageyama et al., 2018). Examining simulations with the same model version ensures that model differences are not responsible for differences between climate states. To explicitly include transient eddy contributions in our analysis, we require daily output from simulations for the LGM, midH, and a high CO_2 state.

Table 1: Boundary conditions in the piControl, LGM, and midH experiments (following Kageyama et al., 2018). The construction of the employed ice sheet history for the LGM is described in Argus et al. (2014); Peltier et al. (2015).

	piControl	LGM	midH
Orbital parameters			
Eccentricity	0.016764	0.018994	0.018682
Obliquity	23.459°	22.949°	24.105°
Perihelion-180	100.33	114.42	0.87
Greenhouse gases (GHGs)			
CO_2 (in ppm)	284.3	190	264.4
CH_4 (in ppb)	808.2	375	597
N_2O (in ppb)	273.0	200	262
Ice sheet topographies	PI	ICE-6G_C	PI

MPI-ESM1.2 is a state-of-the-art coupled Earth system model that was developed at the Max-Planck-Institute for Meteorology in Hamburg. It consists of general circulation models for the atmosphere (ECHAM6.3) and ocean (MPIOM1.63) which exchange energy, mass, and momentum through the OASIS coupler. Land surface processes, including vegetation, are simulated by the land surface model JSBACH3.20, while ocean biogeochemistry is modeled by the HAMOCC6 module. The model configuration analyzed here is the low resolution (LR) configuration (atmospheric resolution: T63, ~200 km; oceanic resolution: ~150 km). The equilibrium climate sensitivity of this model version is 2.83 K (Mauritsen et al., 2019).

We investigate means over 30 year periods of the r1i1p1f1 ensemble member from the MPI-ESM1.2-LR piControl (Wieners et al., 2019a), LGM (Jungclaus et al., 2019a), midH (Jungclaus et al., 2019b) and abrupt4xCO$_2$ (Wieners et al., 2019b) simulations, respectively. We use the first 30 years from the PI, LGM, and midH simulations, and the last 30 years from the 4xCO$_2$ simulation. The most relevant boundary conditions that differentiate the PI, LGM and midH experiments are summarized in Table 1 (Kageyama et al., 2017; Otto-Bliesner et al., 2017). The 4xCO$_2$ experiment branches from the PI simulation: the PI CO$_2$ concentration was immediately and abruptly quadrupled and then held fixed throughout the simulation, while all other boundary conditions were fixed at PI conditions (Eyring et al., 2016). Evaluations against paleoclimate proxy data show that the midH and LGM simulations with MPI-ESM1.2 have comparable performances to other simulations conducted within the PMIP3 and PMIP4 projects (Brierley et al., 2020; Kageyama et al., 2021).

3 Methods

We draw on a moisture budget decomposition, which first decomposes $P - E$ changes into mean circulation and transient eddy terms, and then splits the mean circulation component into thermodynamic, dynamic, and non-linear contributions. Lastly, we estimate the importance of surface temperatures and relative humidity changes for the thermodynamic contributions by employing a slightly modified version of the extended thermodynamic scaling from Byrne and O'Gorman (2015).

3.1 Moisture budget decomposition

In a steady state, in which changes in atmospheric moisture storage are negligibly small, the difference between precipitation (P) and evapotranspiration (E), $P - E$, is balanced by the convergence of the vertically integrated horizontal moisture flux $\mathbf{F}$ (Trenberth and Guillemot, 1995). Thus, the change (Δ) in $P - E$ between two steady states can be written as

$$\Delta(P - E) = -\nabla \cdot (\Delta \mathbf{F}).$$ (1)

where $\mathbf{F}$ is defined as

$$\mathbf{F} = \frac{1}{g} \int_0^{p_s} (\mathbf{u} \cdot q) \, dp, \tag{2}$$

with p_s the surface pressure, g the gravitational acceleration, q the specific humidity and $\mathbf{u} = (u, v)$ the horizontal wind vector.

Indicating monthly means with overbars, climatological monthly means with double overbars, departures of daily means from climatological monthly means with primes and departures of monthly means from climatological monthly means with hats (following the notation by Lora, 2018), we split the moisture flux into three components:

$$\overline{\overline{\mathbf{F}}} \approx \overbrace{\frac{1}{g} \int_0^{p_s} \left(\overline{\overline{\mathbf{u}}} \cdot \overline{\overline{q}} \right) dp}^{\mathbf{F}_{\text{mean}}} + \overbrace{\frac{1}{g} \int_0^{p_s} \overline{\overline{(\mathbf{u}' \cdot q')}} dp}^{\mathbf{F}_{\text{eddy}}} + \overbrace{\frac{1}{g} \int_0^{p_s} \overline{\overline{(\hat{\mathbf{u}} \cdot \hat{q})}} dp}^{\mathbf{F}_{\text{intvar}}}. \tag{3}$$

The respective convergences of changes in these three moisture flux components represent contributions to $\Delta(P - E)$ from changes in the climatological monthly mean $\mathbf{u}$ and q (ΔMEAN), submonthly (transient) eddies (ΔSME), and the covariance of monthly mean $\mathbf{u}$ and q anomalies (named ΔIntVar as it relates to inter-annual variability of $\mathbf{u}$ and q):

$$\Delta \overline{\overline{(P - E)}} \approx \Delta\text{MEAN} + \Delta\text{SME} + \Delta\text{IntVar}, \tag{4}$$

$$\Delta\text{MEAN} = -\nabla \cdot \frac{1}{g} \int_0^{p_s} \Delta \left(\overline{\overline{\mathbf{u}}} \cdot \overline{\overline{q}} \right) dp, \tag{5}$$

$$\Delta\text{SME} = -\nabla \cdot \frac{1}{g} \int_0^{p_s} \Delta \overline{\overline{(\mathbf{u}'q')}} dp, \tag{6}$$

$$\Delta\text{IntVar} = -\nabla \cdot \frac{1}{g} \int_0^{p_s} \Delta \overline{\overline{(\hat{\mathbf{u}} \cdot \hat{q})}} dp. \tag{7}$$

Following Seager et al. (2010) and Byrne and O'Gorman (2015), ΔMEAN can be further split into thermodynamic, dynamic and nonlinear terms, which separate the influence of circulation and specific humidity changes:

$$\Delta\text{MEAN} = \Delta\text{MTh} + \Delta\text{MDyn} + \Delta\text{MNL}, \tag{8}$$

$$\Delta\text{MTh} = -\nabla \cdot \frac{1}{g} \int_0^{p_s} \left(\overline{\overline{\mathbf{u}}}_{\text{PI}} \cdot \Delta\overline{\overline{q}} \right) dp, \tag{9}$$

$$\Delta\text{MDyn} = -\nabla \cdot \frac{1}{g} \int_0^{p_s} \left(\Delta\overline{\overline{\mathbf{u}}} \cdot \overline{\overline{q}}_{\text{PI}} \right) dp, \tag{10}$$

$$\Delta\text{MNL} = -\nabla \cdot \frac{1}{g} \int_0^{p_s} \left(\Delta\overline{\overline{\mathbf{u}}} \cdot \Delta\overline{\overline{q}} \right) dp. \tag{11}$$

In deriving Eq. (3) and (4), we omit daily and monthly fluctuations in surface pressure which are assumed to contribute very little to climatological $P - E$ changes (Seager and Henderson, 2013).

3.2 Thermodynamic scaling

To further examine the thermodynamic contributions to $\Delta P - E$, we employ the extended thermodynamic scaling introduced by Byrne and O'Gorman (2015). It explains the thermodynamic contributions to the moisture budget by changes in local temperature and relative humidity as well as their spatial gradients. Byrne and O'Gorman (2015) assume that $\mathbf{F}_{\text{mean}}$ scales with near-surface specific humidity and that $\mathbf{F}_{\text{eddy}}$ and $\mathbf{F}_{\text{intvar}}$ scale with the gradient in near-surface specific humidity. Substituting these assumptions into Eq. (1) and decomposing specific humidity changes into relative humidity and temperature contributions through the Clausius-Clapeyron relationship between saturation water vapour pressure and temperature, Byrne and O'Gorman (2015) obtain the following approximation for the combined thermodynamic contributions ΔTh to ΔMEAN, ΔSME, and ΔIntVar:

$$\Delta\overline{\overline{Th}} \approx \overline{\overline{\alpha}}_{\text{PI}} \Delta\overline{\overline{T}}_s \cdot \overline{\overline{(P - E)}}_{\text{PI}} + \frac{\Delta\overline{\overline{RH_s}}}{\overline{\overline{RH_{s_{\text{PI}}}}}} \cdot \overline{\overline{(P - E)}}_{\text{PI}} - \mathbf{G}_{\text{PI}} \cdot \nabla \left(\overline{\overline{\alpha}}_{\text{PI}} \Delta\overline{\overline{T}}_s \right) - \mathbf{G}_{\text{PI}} \cdot \nabla \left(\frac{\Delta\overline{\overline{RH_s}}}{\overline{\overline{RH_{s_{\text{PI}}}}}} \right). \tag{12}$$

Here, RH_s stands for the near-surface relative humidity, T_s for the near-surface temperature, $\mathbf{G}$ for the modified moisture flux, defined as[1]

$$\mathbf{G} = \mathbf{F}_{\text{mean}} + 2 \cdot (\mathbf{F}_{\text{eddy}} + \mathbf{F}_{\text{intvar}}), \tag{13}$$

and α for the Clausius-Clapeyron scaling coefficient, defined as

$$\alpha = \frac{L}{R_v \cdot T_s^2}, \tag{14}$$

where L is the latent heat of vaporization and sublimation, and R_v the gas constant of water vapour. Note that the first term of Eq. (12), henceforth referred to as the local temperature term, corresponds to the simple thermodynamic scaling derived by Held and Soden (2006). Furthermore, we call the second term of Eq. (12) the local relative humidity term, while the third and fourth terms will respectively be referred to as the temperature and relative humidity gradient terms. A detailed derivation of the four terms is given in Byrne and O'Gorman (2015).

To directly compare the results of the thermodynamic approximation with ΔMTh, we additionally compute the following version of the extended scaling, which neglects transient eddy contributions to $P - E$ and its changes:

$$\Delta\text{MTh} \approx \overline{\overline{\alpha}}_{\text{PI}} \, \Delta\overline{\overline{T}}_s \cdot \left(-\nabla \cdot \mathbf{F}_{\text{mean}_{\text{PI}}} \right) + \frac{\Delta\overline{\overline{RH_s}}}{\overline{\overline{RH_{s_{\text{PI}}}}}} \cdot \left(-\nabla \cdot \mathbf{F}_{\text{mean}_{\text{PI}}} \right)$$

$$- \mathbf{F}_{\text{mean}_{\text{PI}}} \cdot \nabla \left(\overline{\overline{\alpha}}_{\text{PI}} \, \Delta\overline{\overline{T}}_s \right) - \mathbf{F}_{\text{mean}_{\text{PI}}} \cdot \nabla \left(\frac{\Delta\overline{\overline{RH_s}}}{\overline{\overline{RH_{s_{\text{PI}}}}}} \right) \tag{15}$$

3.3 Numerical implementation

We evaluate vertical integrals by first interpolating linearly to a high vertical resolution and extrapolating linearly to p_s if p_s is higher than the largest available pressure level, before computing midpoint Riemann sums. If, in a simulation, no data are available for a pressure level (i.e., the pressure level would be below the surface), we set $q = 0$ and $\mathbf{u} = 0$ in the computation of the integral. This case is most relevant in areas where melting ice sheets since the LGM caused increased surface pressure.

We compute spatial gradients using a second order central finite difference approximation. Only for the most pole-ward grid boxes, first order forward/backward approximations are used in the meridional direction. The differentiation is not performed on the native grid of the model. This creates small-scale numerical artefacts. We reduce them by applying a spatial smoothing with a 3x3 quadratic kernel to gradient terms. We compute submonthly eddy terms from the archived daily mean values, thereby neglecting subdaily co-variability of q and $\mathbf{u}$. All other terms are computed from monthly mean simulation output due to the availability of data for more vertical levels.

As the numerical implementation is not exact (for a detailed analysis, see Seager and Henderson, 2013), we denote the sum of the terms on the right hand side of Eq. (4) by $\Delta(P - E)^*$. This emphasizes the difference between $\Delta(P - E)$ and its approximate decomposition. The large-scale agreement between annual mean $\Delta(P - E)$ and $\Delta(P - E)^*$ is very high (Supplemental Text S2, Fig. S1).

3.4 Spatial correlations between fields

We report the area-weighted Pearson r as a measure for the spatial correlation between two fields. Confidence intervals are derived from Fisher's z statistic which depends on the degrees of freedom in the data. To accommodate for the spatial autocorrelation in the fields, we determine the spatial decorrelation length of $\Delta(P - E)$ for LGM, 4xCO$_2$, and midH using semi-variograms (Di Cecco and Gouhier, 2018; Lakhankar et al., 2010; van de Beek et al., 2011). Specifically, we determine the sill position in semi-variograms for different latitude ranges (Text S3, Fig. S2). Interpreting the sill

---

[1] Byrne and O'Gorman (2015) do not separate between $\mathbf{F}_{\text{eddy}}$ and $\mathbf{F}_{\text{intvar}}$.

position as the decorrelation length d^* of the spatial autocorrelation in $P-E$, we define the degrees of freedom as the area of the region of interest divided by the area of a circle with radius $\frac{d^*}{2}$. For global fields, we obtain on average 104 degrees of freedom. We use the same effective degrees of freedom for all contributions to the moisture budget.

4 Results

In this section, we first summarize the patterns of $P-E$ changes for the LGM, midH and 4xCO$_2$ states (Sect. 4.1). Then, we examine the state dependency and state invariance of the patterns and relative importance of the moisture budget decomposition terms (Sect. 4.2). We further analyze the rates of decay of moisture budget terms on large spatial scales and potential global mean compensations between contributions. Third, we investigate the thermodynamic contributions in more detail using the thermodynamic scaling (Sect. 4.3). Finally, combining moisture budget and thermodynamic scaling terms, we test the applicability of the WWDD/DWWD paradigm (Sect. 4.4). We assess the viability of the LGM as a cold world analog by comparing all results for LGM and 4xCO$_2$. Throughout this section, we compare climatological annual mean anomalies of the LGM, 4xCO$_2$, and midH simulations from the PI simulation unless stated otherwise. We mostly separate analyses of land and ocean areas due to their differing surface properties.

4.1 Precipitation minus evapotranspiration changes

The annual mean $\Delta(P-E)$ pattern of 4xCO$_2$ displays overall wetting in the inner tropics and mid-to-high latitudes and drying in the subtropics, with zonally more homogeneous structures over oceans than over land (Fig. 1). Compared to 4xCO$_2$, the LGM anomalies are zonally less homogeneous in the Northern Hemisphere (NH) mid-latitudes and hemispherically anti-symmetric in the tropical Pacific. Therefore, the spatial anticorrelation between LGM and 4xCO$_2$ anomalies is small ($r = -0.16 \pm 0.16$[2]). Nevertheless, the LGM and 4xCO$_2$ anomalies feature an opposing sign for 65% of the global area (termed 'sign opposition' in the following) and in 45 out of 58 reference regions used in the Sixth Assessment Report (AR6) of the IPCC WG1[3] (see Fig. 4 for definition of the regions). $P-E$ changes for the midH are smaller than for the LGM and 4xCO$_2$. MidH $\Delta(P-E)$ magnitudes are highest over tropical oceans and mostly weak in the extratropics. The largest changes over land are drying over northern South America and wetting over south-eastern Asia.

To test the robustness of the diagnosed regional $P-E$ changes with respect to the selected 30 year intervals, we compare the $\Delta(P-E)$ changes with the ones obtained for other 30 year intervals of the available simulation output (200 years for PI, midH and LGM, 165 years for 4xCO$_2$). Note that the climate state of the 4xCO$_2$ simulation converges towards a new equilibrium during the simulation, such that larger differences are expected than for the other simulations. Therefore, we focus on identifying regions that display a mismatch in sign of $\Delta(P-E)$ for alternative 30 year periods (Fig. S3). For LGM and 4xCO$_2$, this affects only a few unconnected regions (7 for LGM, 9 for 4xCO$_2$), while 26 out of 58 AR6 reference regions are concerned for midH due to small $P-E$ changes in the extratropics. This indicates that for LGM and 4xCO$_2$, the direction of $P-E$ changes is a robust signal for the large majority of regions. We additionally note that in all regions with sign changes for alternative 30 year periods, the absolute regional mean anomalies are small (< 0.26 mm/day).
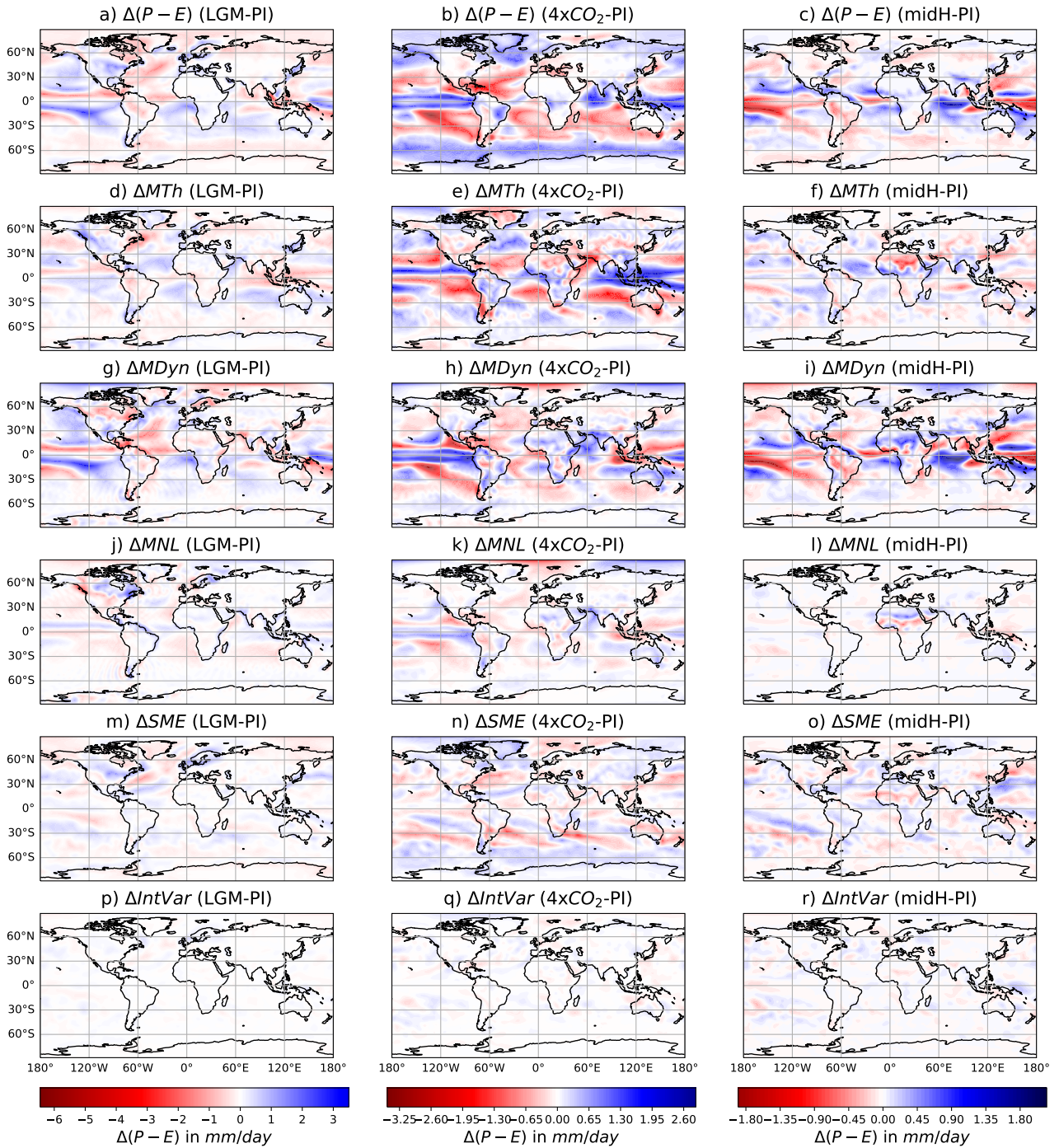
Figure 1: Mean annual moisture budget changes of LGM (left column), 4xCO$_2$ (middle column) and midH (right column) from PI. We show (a-c) precipitation minus evaporation ($\Delta P - E$), and (d-f) climatological monthly mean thermodynamic (ΔMTh), (g-i) climatological monthly mean dynamic (ΔMDyn), (j-l) climatological monthly mean non-linear (ΔMNL), (m-o) submonthly eddy (ΔSME) and (p-r) inter-annual co-variability (ΔIntVar) contributions to the $P - E$ changes. All terms are smoothed using a spatial 3x3 quadratic kernel. Note that the value ranges differ between states.
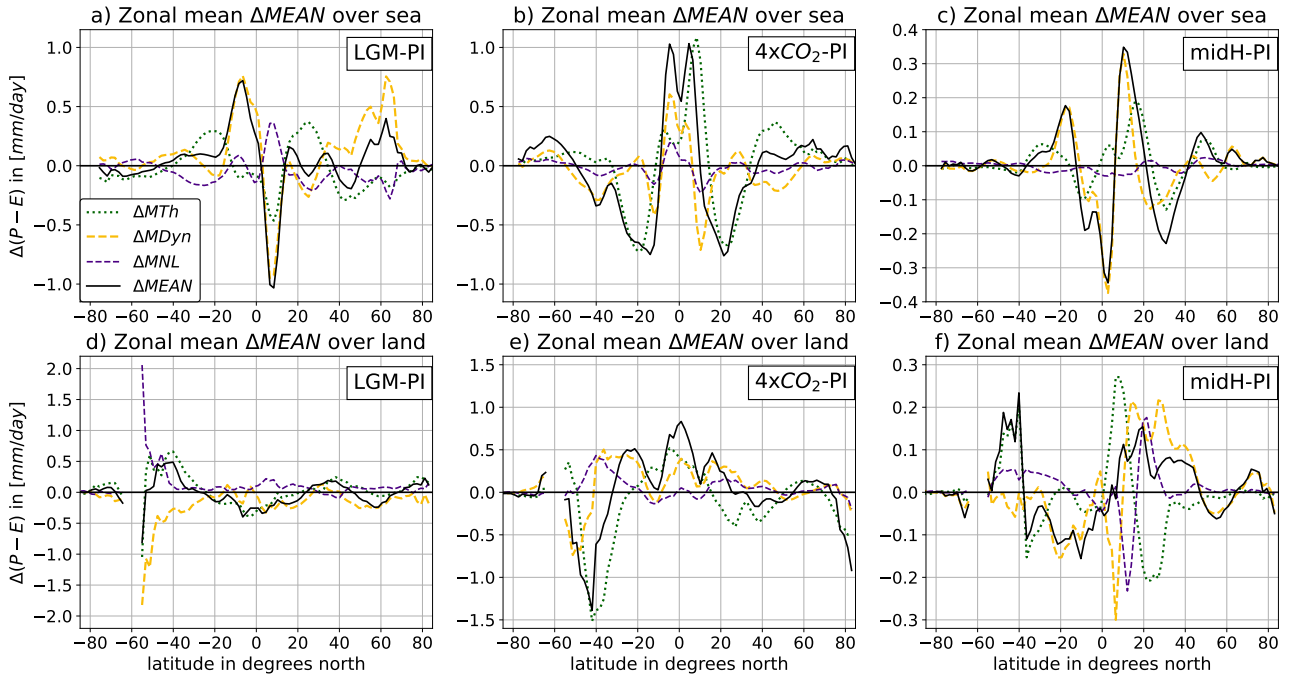
Figure 2: Zonal mean annual mean thermodynamic (ΔMTh), dynamic (ΔMDyn) and nonlinear (ΔMNL) contributions to ΔMEAN over (a-c) ocean and (d-f) land.

4.2 Moisture budget decomposition

4.2.1 Patterns of dynamic, thermodynamic and nonlinear climatological monthly mean contributions

For $P - E$ changes related to the climatological monthly mean flow (ΔMEAN), the moisture budget decomposition (Eq. 8) distinguishes thermodynamic (ΔMTh), dynamic (ΔMDyn) and nonlinear (ΔMNL) contributions (Fig. 1d-l, Fig. 2). Here, we analyze the similarity of signs and patterns between the three states and the overall consistency of relationships between the three terms across states.

Over the ocean, we find zonally homogeneous ΔMTh patterns for the LGM, with drying in the inner tropics, wetting in the subtropics, and drying in the mid- and high latitudes. These patterns are mostly reversed for $4xCO_2$ ($r = -0.73 \pm 0.11$, 78.5% sign opposition), with strongest anticorrelation in the tropics. In contrast, ΔMTh for the midH tends to be hemispherically anti-symmetric, in line with the opposing insolation anomalies between NH and SH. Conversely, the dynamic patterns (ΔMDyn) over the ocean differ strongly between LGM and $4xCO_2$ ($r = 0.07 \pm 0.20$, 55% sign opposition), with hemispherically anti-symmetric patterns for the LGM compared to symmetric patterns for $4xCO_2$. For the midH, a dynamic zonal mean drying near the equator is counteracted by zonal mean wetting in the NH outer tropics, especially in the Pacific. The nonlinear term ΔMNL tends to be much smaller in magnitude than ΔMTh and ΔMDyn for all three investigated cases. For $4xCO_2$, ΔMNL displays a similar pattern as ΔMDyn ($r = 0.90 \pm 0.05$), whereas ΔMNL and ΔMDyn tend to counteract each other for the LGM ($r = -0.47 \pm 0.17$). In contrast, the relation between ΔMNL and ΔMDyn is strongly regionally dependent for the midH. The strong positive correlation with ΔMDyn for $4xCO_2$ and negative correlation for the LGM indicates that the dynamic term imprints its pattern onto the nonlinear term, while the sign of the correlation is determined by the specific humidity changes which are mostly positive for $4xCO_2$ and negative for the LGM.

---

[2]Reported uncertainties correspond to 90% confidence intervals unless stated otherwise.

[3]The IPCC AR6 WG1 defines 58 reference regions based on climatic homogeneity and representation of regional climate features, including mean temperature and precipitation (Iturbide et al., 2020). We compute area-weighted regional means for each of the regions.
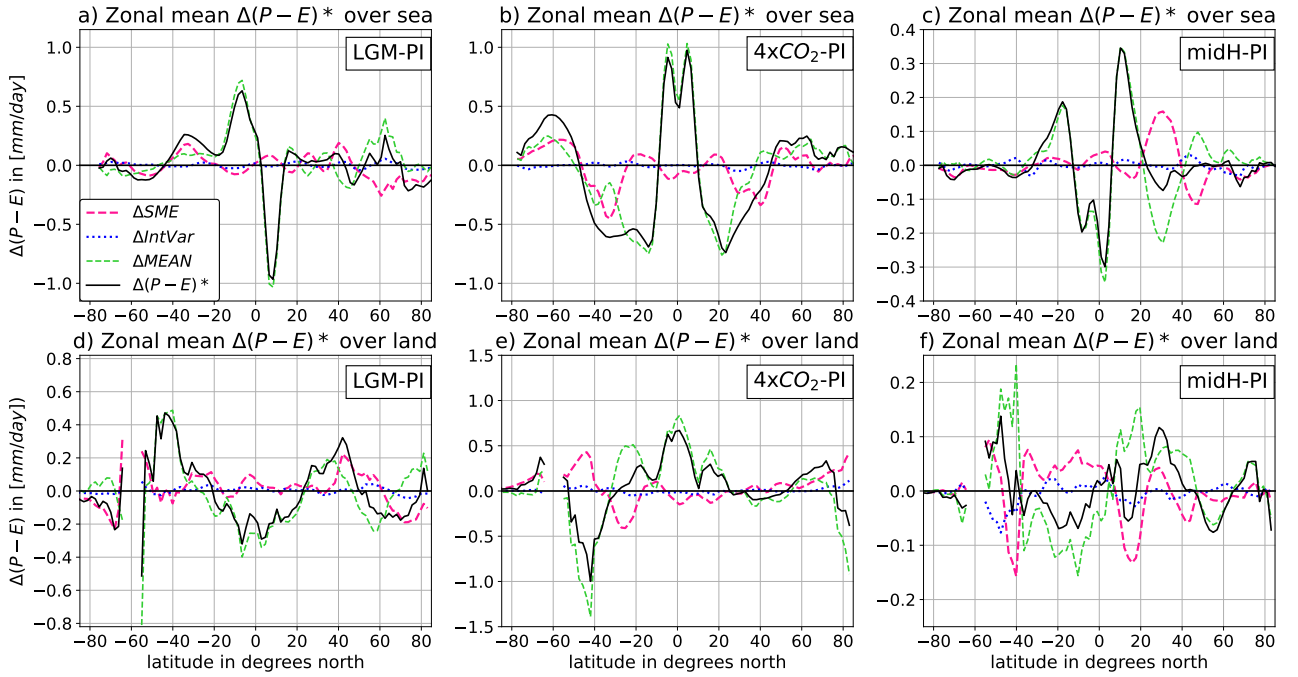
Figure 3: Zonal mean annual mean ΔMEAN, ΔSME, and ΔIntVar contributions, and their sum $\Delta(P-E)$* over (a-c) ocean and (d-f) land.

Over land, $P - E$ changes are generally more regionalized: for the LGM, we find thermodynamic wetting over ice sheets and drying over northern Eurasia downstream of the Fennoscandian ice sheet. Meanwhile, extratropical zonal mean changes are stronger for the dynamic term due to large-scale drying over the LGM ice sheets. For $4xCO_2$, ΔMTh and ΔMDyn are zonally more homogeneous than for the LGM, with wetting over tropical land for both terms and thermodynamic (dynamic) drying (wetting) at mid-latitudes and thermodynamic (dynamic) wetting (drying) at high latitudes. The thermodynamic terms of LGM and $4xCO_2$ are also negatively correlated over land ($r = -0.54 \pm 0.26$, 78.7% sign opposition), but weaker than over the ocean. Similarly, there is no significant correlation between the ΔMDyn terms for LGM and $4xCO_2$ ($r = -0.11 \pm 0.32$, 60.8% sign opposition). For the midH, the strongest changes are dynamic drying in tropical South America and dynamic wetting in North Africa. The latter is partly compensated by thermodynamic drying. Similar to the results over oceans, ΔMNL and ΔMDyn strengthen each other over land for $4xCO_2$ ($r = 0.71 \pm 0.20$), while they weaken each other for the LGM ($r = -0.64 \pm 0.23$). This is especially noticeable over the LGM ice sheets, where ΔMNL of the LGM reaches its highest magnitudes. Taking land and ocean together, we find that ΔMTh and ΔMDyn tend to weaken each other for $4xCO_2$ ($r = -0.49 \pm 0.13$). There is, however, no clear relationship between ΔMTh and ΔMDyn for the LGM ($r = 0.01 \pm 0.16$). For midH, ΔMTh and ΔMDyn are negatively correlated over land ($r = -0.55 \pm 0.26$) but not over oceans.

In summary, we find opposing patterns between LGM and $4xCO_2$ for ΔMTh, especially over oceans, but not for ΔMDyn. While there is a consistent relationship between ΔMDyn and ΔMNL for LGM and $4xCO_2$ when taking the opposing signs of thermodynamic changes into account, the relationship between ΔMTh and ΔMDyn is state-dependent. In general, changes are more regionalized over land, similar to the overall $P - E$ changes.

4.2.2 Patterns of submonthly eddy and inter-annual co-variability contributions

In addition to climatological monthly mean flow contributions (ΔMEAN, Eq. 5), $P - E$ also changes due to submonthly eddy (ΔSME, Eq. 6), and interannual co-variability contributions (ΔIntVar, Eq. 7). Here, we analyze the relationships between ΔMEAN, ΔSME, and ΔIntVar across states, and the similarity of ΔSME patterns between the states.

For all three cases, the strongest ΔSME contributions are found in the extratropics (Fig. 1m-o, Fig. 3).

11

Table 2: Number of regions with dominant thermodynamic (first row), dynamic (second row), and non-linear (third row) contribution to ΔMEAN for LGM, 4xCO$_2$, and midH. The last two columns refer to the number of regions with dominant ΔMTh/ΔMDyn/ΔMNL contributions for both, LGM and 4xCO$_2$, and for all three states, respectively.

	LGM	4xCO$_2$	midH	LGM & 4xCO$_2$	LGM & 4xCO$_2$ & midH
ΔMTh	14	26	12	11	2
ΔMDyn	22	15	31	12	7
ΔMNL	1	2	1	0	0

Over the SH oceans, ΔSME of LGM (4xCO$_2$) causes zonal mean wetting (drying) between 20°S - 40°S and drying (wetting) between 40°S - 60°S. In contrast, the patterns over NH oceans differ more between LGM and 4xCO$_2$ with zonally more tilted bands for the LGM. Over land, ΔSME shows strongly regionalized features with LGM wetting over the Laurentide ice sheet and 4xCO$_2$ wetting over Greenland being the most prominent ones. For the midH, ΔSME displays zonally heterogeneous patterns over the ocean, whereas it contributes to widespread wetting over SH subtropical land regions and drying over North Africa.

ΔMEAN and ΔSME tend to counteract each other for all three cases with an opposition in sign for $\sim$67% of the global area and significant anticorrelation for all three scenarios (LGM: $r = -0.45 \pm 0.14$, 4xCO$_2$: $r = -0.39 \pm 0.15$, midH: $r = -0.59 \pm 0.12$). Comparing ΔSME of the LGM and 4xCO$_2$, we find opposition in sign for 60% of the ocean area and 68.9% of the land area, but only weak spatial anticorrelation ($r = -0.23 \pm 0.16$). ΔIntVar is generally of much smaller magnitude than the other terms of the moisture budget (Fig. 1p-r, Fig. 3). However, we find that ΔIntVar tends to support ΔSME, as both terms agree in sign for $\sim$ 62% of the global area for the LGM, 4xCO2, and the midH. Taken together, we find consistent relationships between ΔMEAN, ΔSME, and ΔIntVar across the three states. Moreover, there is a weak but statistically significant opposition in the ΔSME patterns between LGM and 4xCO$_2$.

4.2.3 Relative importance of moisture budget contributions

We next assess the relative importance of the moisture budget contributions in different regions and compare them between the three states. For a total of n contribution terms x_i, with $i = 1, 2, ... n$, the relative importance c_i of each term x_i for a certain region (in percent) is quantified as follows:

$$c_i = 100 \cdot \frac{|x_i|}{\sum_{i=1}^{n} |x_i|}. \tag{16}$$

Depending on the sign of x_i, we call its relative contribution wet or dry. We define a term as dominant if its relative regional mean contribution surpasses 50%. This condition can be fulfilled by at most one contribution per region, which is then also decisive for the sign of the regional mean anomaly. We compute c_i for 56 of the 58 AR6 reference regions, excluding East Antarctica and the Arctic ocean due to numerical artefacts.

We first compare the relative importance of the thermodynamic, dynamic and nonlinear contribution for determining the sign of ΔMEAN (Fig. 4, Table 2). For 4xCO$_2$, we find about twice as many thermodynamically dominated regions as for the LGM and the midH. Conversely, the LGM and especially the midH feature more dynamically dominated regions than 4xCO$_2$. Comparing the LGM and 4xCO$_2$, we particularly detect a tendency towards higher relative importance of ΔMTh and lower relative importance of ΔMDyn for 4xCO$_2$ in regions covered by ice sheets during the LGM. Moreover, regions with the same dominant contribution term in both states are in the minority. Dynamic dominance prevails over the Pacific, the North Atlantic and nearby regions, while the thermodynamic term is found to be dominant in vicinity of the Southern and Indian Ocean, as well as over six
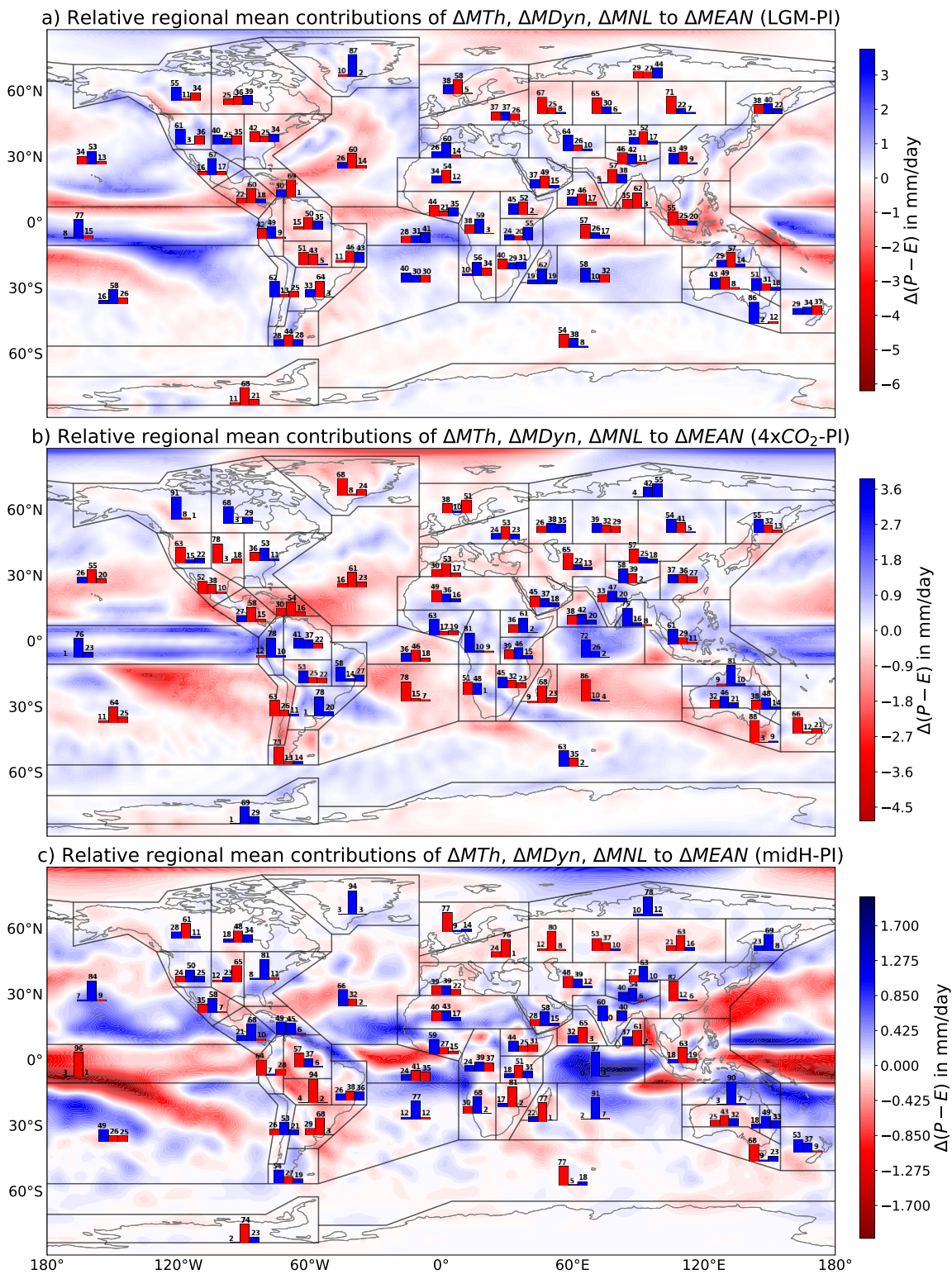
Figure 4: Annual mean ΔMEAN of (a) LGM, (b) 4xCO₂, (c) midH with histograms indicating the wet (in blue) and dry (in red) relative regional mean contributions of ΔMTh, ΔMDyn and ΔMNL to regional mean ΔMEAN (from left to right, given in %). Note that the percentages are rounded and therefore do not always add up to 100%.
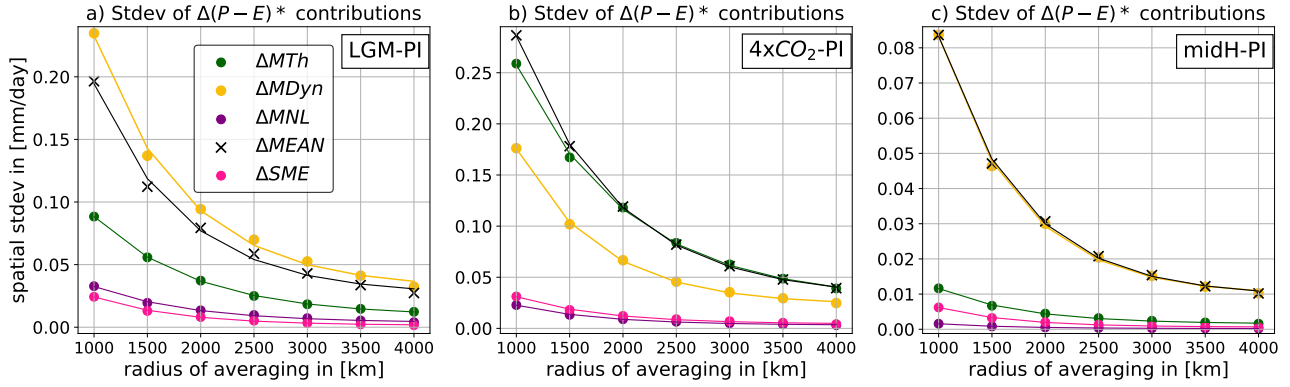
Figure 5: Spatial standard deviation of contributions to the annual mean moisture budget for different radii of averaging. Lines correspond to exponential fits of the decay for increasing averaging scales. ΔIntVar is not shown because of its very small amplitudes.

unconnected land regions. A three-way comparison finally reveals that the dominance of the same contribution for all investigated climate states only holds true for a very small number of isolated regions. In accordance with its predominantly lower amplitude, ΔMNL is dominant in the fewest number of regions for all climate states.

We further examine the relative importance of climatological monthly mean (ΔMEAN), submonthly eddy (ΔSME), and interannual co-variability (ΔIntVar) contributions for determining the regional mean sign of their sum $\Delta(P - E)^*$, which closely approximates $\Delta(P - E)$. For all three states, regional mean ΔMEAN is the dominant contribution for the majority of the 56 investigated regions (39 for LGM, 36 for 4xCO$_2$, 42 for midH). ΔSME dominates for 14 regions for the LGM and 4xCO$_2$, and 4 for the midH. Most of these regions are extratropical land regions, but they predominantly differ between states. While 20 regions feature dominant ΔMEAN for all three states, no region is dominated by ΔSME for all three states. As expected from its mostly negligible contribution, ΔIntVar is dominant in none of the regions for LGM and 4xCO$_2$ and only three regions for midH.

In summary, we find strong differences in the relative importance of ΔMTh, MDyn, and ΔMNL between the three states. In contrast, the large-scale importance of ΔMEAN, ΔSME, and ΔIntVar is fairly consistent between states, despite differences in the specific regions where ΔSME dominates.

4.2.4 Closure and decay of moisture budget contributions on large spatial scales

Because $P - E$ and therefore $\Delta(P - E)$ vanish in the global mean due to the closure of the moisture budget, the moisture budget terms have to compensate each other in the global mean. To quantify the extent of this compensation, we compute the global means of the moisture budget decomposition terms ΔMEAN, ΔMTh, ΔMDyn, ΔMNL, ΔSME, and ΔIntVar. We find that all six terms vanish in the global mean for all three states (Table S1). This means that no compensation of the terms is required on the global-scale to close the $P - E$ budget.

We additionally examine the rates of decay of the contributions towards zero for larger spatial scales. To this purpose, we average the terms over circles with increasing radii centered at each grid point and compute the spatial variability of the smoothed fields. We find a steady variability decrease for all moisture budget terms towards larger smoothing scales (Fig. 5). This is expected as the spatial variability is zero for radii including the whole Earth. However, we also find remarkably similar rates of decay: for all components of the moisture budget and all three climate states, the decrease follows an exponential function with a rate of decay between 0.47 and 0.73 [10^{-3}km^{-1}] (Table S1). These values are similar to the rate of decay for absolute $P - E$ in the four simulations (between 0.36 and 0.43 [10^{-3}km^{-1}]).
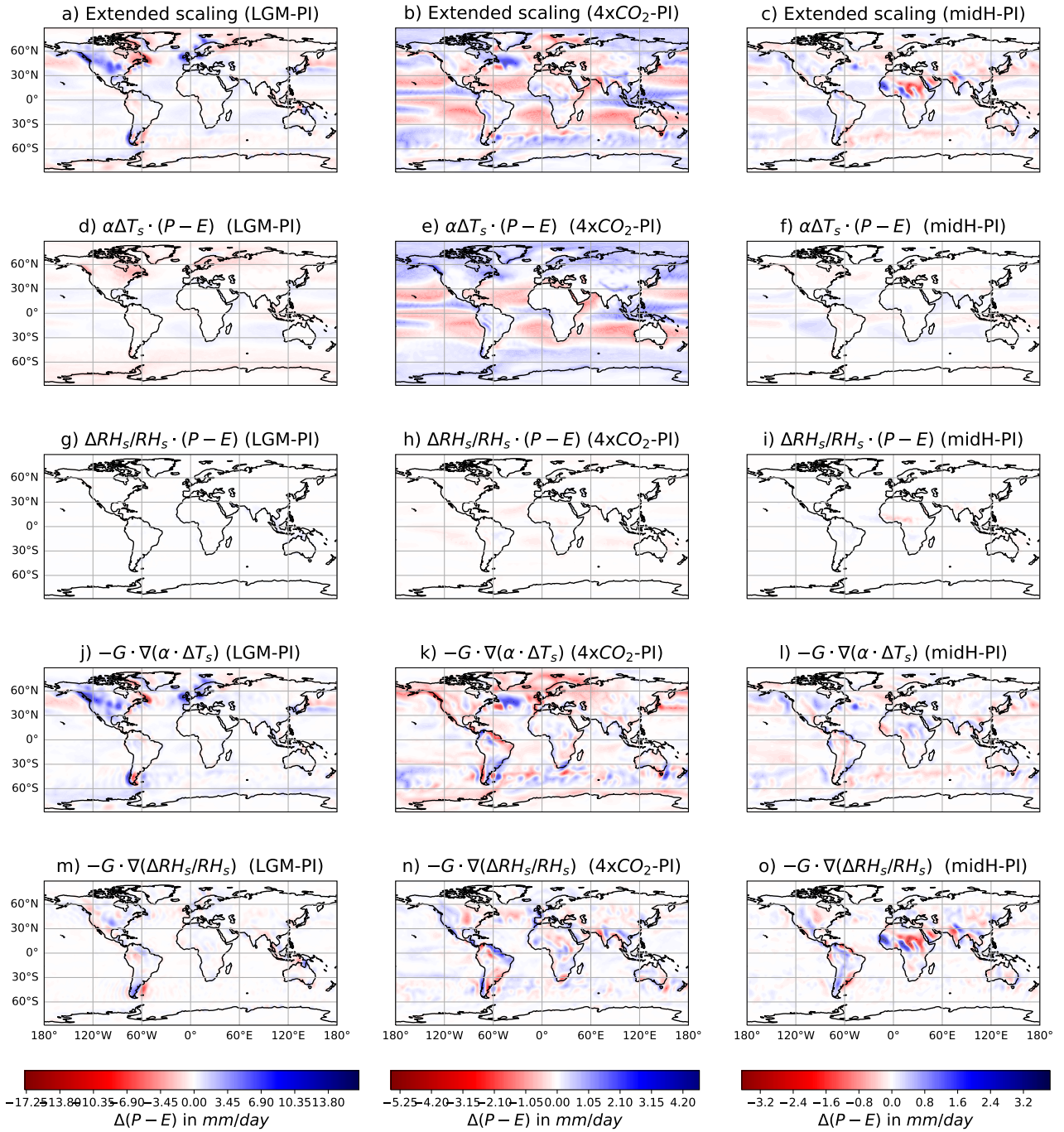
14

Figure 6: (a-c) Annual mean extended thermodynamic scaling and contributions from (d-f) the local temperature term, (h-i) the local relative humidity term, (j-l) the temperature gradient term, and (m-o) the relative humidity gradient term for the LGM (left column), 4xCO₂ (central column), and the midH (right column).
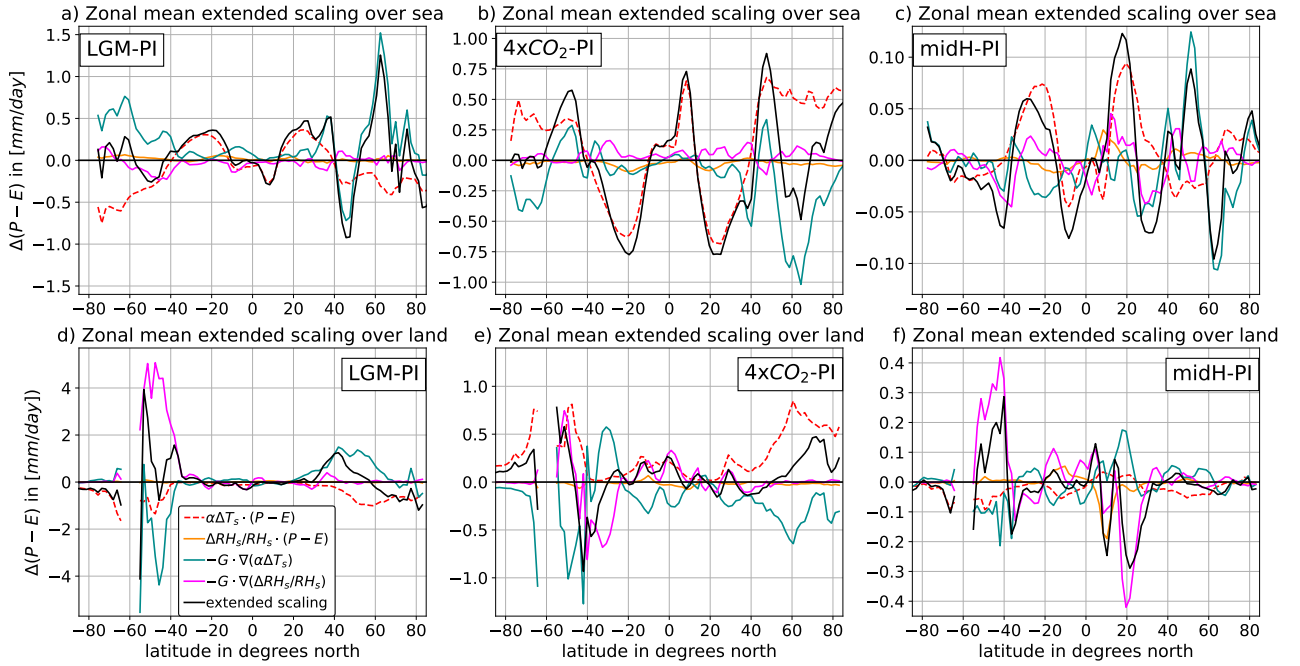
Figure 7: Zonal mean annual mean extended scaling and contributions from the local temperature term, the local relative humidity term, the temperature gradient term, and the relative humidity gradient term for the LGM, 4xCO$_2$, and the midH over (a-c) ocean and (d-f) land.
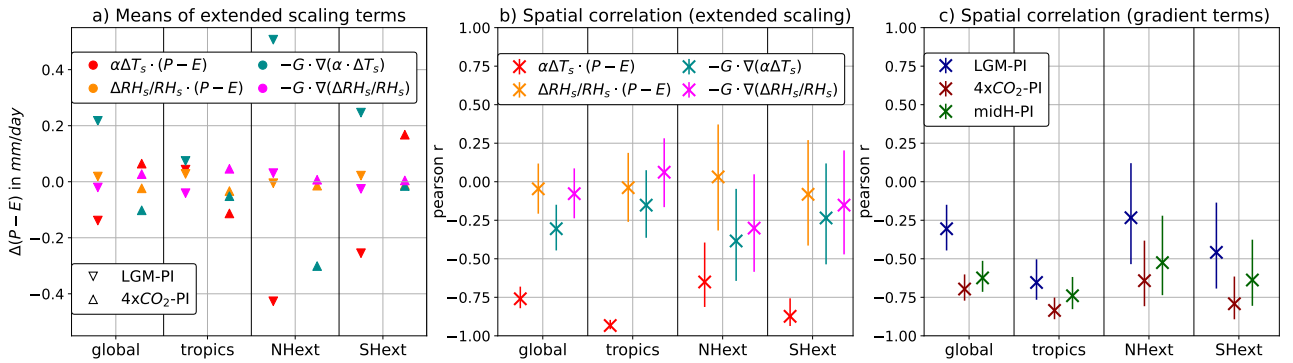

Figure 8: (a) Spatial means of extended scaling terms for LGM and 4xCO$_2$ over the indicated areas. (b) Spatial correlation between annual mean extended scaling terms for LGM and 4xCO$_2$ over the indicated areas. (c) Spatial correlation between annual mean $-\mathbf{G}_{PI} \cdot \nabla(\frac{\Delta RH_s}{RH_s}_{PI})$ (relative humidity gradient term) and annual mean $-\mathbf{G}_{PI} \cdot \nabla(\alpha_{PI} \cdot \Delta T_s)$ (temperature gradient term) for LGM, 4xCO$_2$, and midH over the indicated areas. Estimates for the tropics include all grid boxes between 30°S and 30°N, whereas all other grid boxes are included in estimates for the extratropics (abbrev.: NHext, SHext). Error bars indicate the 90% confidence intervals of spatial correlations.
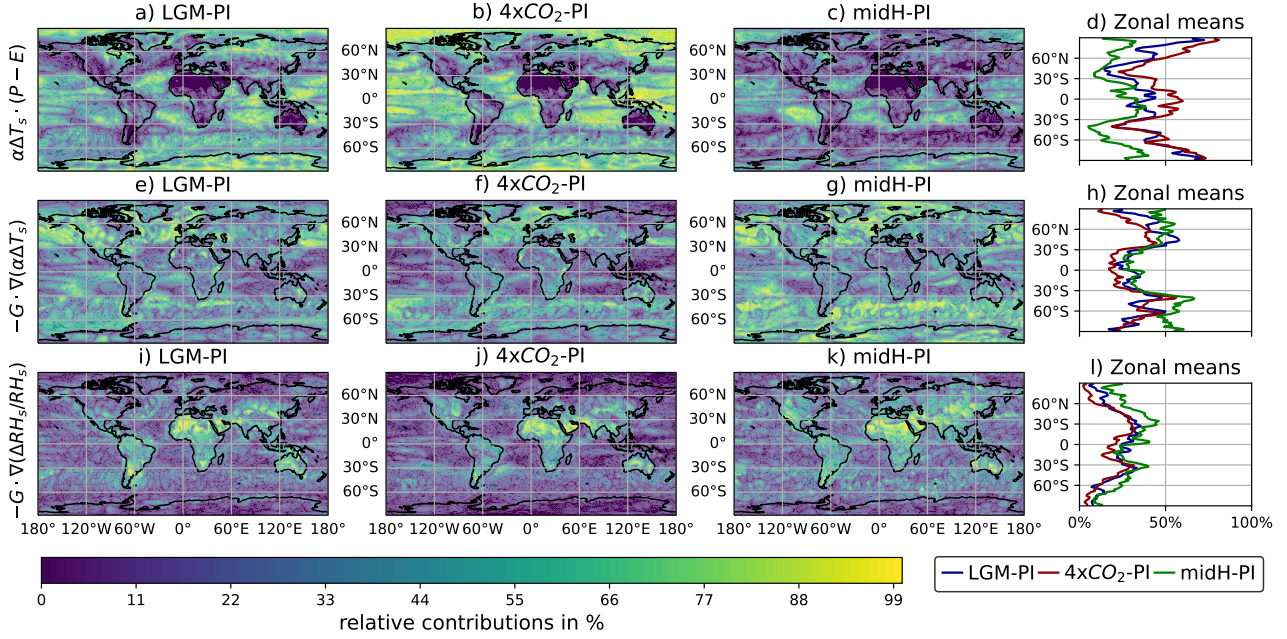
Figure 9: Relative contributions of (a-c) the annual mean local temperature term, (e-g) the temperature gradient term, and (i-k) the relative humidity gradient term to the extended scaling (given in %), and (d, h, l) their zonal means.

4.3 Patterns and relative importance of thermodynamic scaling terms

We apply the extended thermodynamic scaling (Eq. 12) introduced by Byrne and O'Gorman (2015) to analyze the drivers of the thermodynamic contributions ΔTh in more detail (Fig. 6, Fig. 7). Here, we first evaluate the accuracy of the thermodynamic scaling by comparing Eq. (15) with the mean flow component ΔMTh. The sign of the thermodynamic scaling agrees mostly with ΔMTh. However, its amplitudes tend to be overestimated, especially near the LGM ice sheets and over North Africa for the midH (Fig. S4). Regions of overestimated drying and wetting are often located at similar latitudes which leads to substantial compensation effects in the zonal mean. Keeping this in mind, we place our emphasis in the following on the state-dependency of relative importance, sign changes, and zonal mean changes of the individual contributions to the thermodynamic scaling, as well as the relationships between them.

Over oceans, the local temperature term displays a zonally homogeneous pattern which follows the $P - E$ patterns for PI. For the LGM (4xCO_2), this causes drying (wetting) in the inner tropics, wetting (drying) in the subtropics, and drying (wetting) in the mid- to high latitudes. Over land, the contributions of the local temperature terms are almost exclusively drying for the LGM and wetting for 4xCO_2. The most pronounced feature of the midH local temperature term is subtropical wetting over oceans (Fig. 6f). The patterns of the temperature and relative humidity gradient terms are more regionalized than for the local temperature term. The influence of the temperature gradient term is especially pronounced in areas covered by ice sheets during the LGM but not today. Due to the westerly flow, the strongly increased temperature gradients at ice sheet edges lead to a wetting along their western and a drying near their eastern edges. The relative humidity gradient term shows patterns with strong local dipoles of wetting and drying. For the midH and 4xCO_2, it reaches highest magnitudes over tropical land regions, especially drylands, while for the LGM, it shows especially high magnitudes at the transitions to the Patagonian and Laurentide ice sheets. The local relative humidity term is predominantly negligible.

The local temperature term is the only contribution to the extended thermodynamic scaling with strong spatial anticorrelation between the LGM and 4xCO_2 across all latitudes (Fig. 8b). The temperature gradient term is significantly anticorrelated only in the NH extratropics and when considering the whole globe, whereas neither the local relative humidity term nor the relative humidity gradient

term are significantly correlated. This is in concordance with their highly regionalized drying and wetting patterns. Additionally, the temperature gradient and the relative humidity gradient terms are anticorrelated for all three climate states (Fig. 8c). The anticorrelation is strongest in the tropics and weakens especially in the NH extratropics for the LGM. In contrast, no consistent anticorrelation is detected between the local temperature and local relative humidity terms.

Analyzing the importance of the different components in the thermodynamic scaling by computing the relative contribution of each term for each grid box (following Eq. 16), we detect striking similarities between all three states (Fig. 9). The local temperature term is prevalent over the tropics and high latitudes and particularly over oceans in these regions. The temperature gradient term on the other hand dominates in the mid-latitudes, while the relative humidity gradient term is most important in arid subtropical land areas. Thus, unlike for the contributing terms to the moisture budget, the importance of the terms in the thermodynamic scaling is largely consistent across the three states. Another difference between the thermodynamic scaling terms and the moisture budget contributions is that not all of the individual terms of the extended scaling vanish in the global mean (Fig. 8a). The local temperature temperature term provides drying (wetting) for LGM ($4xCO_2$) which is balanced by wetting (drying) from the temperature gradient term. In contrast, the global averages of the relative humidity terms are close to zero. The spatial means of the local temperature and the temperature gradient terms for the LGM and $4xCO_2$ oppose each other in the NH and SH extratropics but not in the tropics.

In summary, we find that the local temperature term is the only term with a strong anticorrelation between $4xCO_2$ and LGM, whereas the temperature gradient and the relative humidity gradient terms are the only consistently anticorrelated terms for all three climate states. Unlike for the terms in the moisture budget decomposition, the patterns of relative importance of the thermodynamic scaling terms are very similar between states and the terms do not vanish in the global mean but compensate each other.

4.4 Testing the wet-get-wetter-dry-get-dryer (WWDD) paradigm

The WWDD paradigm is often postulated as a first order approximation of $P - E$ changes under global warming. For global cooling, it corresponds to a dry-get-wetter-wet-get-dryer (DWWD) pattern. While the limitations of the WWDD paradigm for land areas are well-established (e.g., Byrne and O'Gorman, 2015), we focus on determining the predictive power of the paradigm depending on the location and relative importance of the individual moisture budget and thermodynamic scaling contributions. As the midH does not feature a consistent global warming or cooling pattern, we focus here on the LGM and $4xCO_2$. By comparing the sum of all moisture budget decomposition contributions, $\Delta(P - E)^*$, with $P - E$ in the PI, we identify 35 out of 56 AR6 reference regions that fulfill WWDD for $4xCO_2$ and 36 regions that fulfill DWWD for the LGM. For 29 regions, both, WWDD for $4xCO_2$ and DWWD for the LGM, hold true. We test the statistical significance of these numbers with randomized experiments, in which we randomly assign positive (wetting) and negative (drying) signs to the 56 regions. Then, we compare the results with the sign of $P - E$ (positive=wet, negative=dry) in the PI for the respective regions and count the number of regions for which WWDD, DWWD, or both is fulfilled. We repeat each experiment 10,000 times to obtain robust test statistics. The tests demonstrate that the occurrence of WWDD (DWWD) for at least 35 (36) regions ($p < 0.05$), as well as WWDD and DWWD for at least 29 regions ($p < 0.01$) purely by chance is very unlikely (Fig. S5 a-c).

Next, we test if WWDD (DWWD) for $4xCO_2$ (LGM) is preferably true for regions with dominant thermodynamic contributions, as the paradigm itself is deduced from the simple thermodynamic scaling. By exclusively comparing ΔMEAN and $(P - E)_{mean}$(PI), we find that WWDD for $4xCO_2$ holds true for 35 regions, including 24 of 26 ΔMTh dominated regions and 7 of 15 ΔMDyn dominated regions. For the LGM, DWWD is found for 37 regions, among them 13 of 14 ΔMTh dominated regions and 13 of 22 ΔMDyn dominated regions. We repeat our statistical experiments for the ΔMTh dominated regions, this time comparing the randomly assigned wetting and drying to the sign of $(P - E)_{mean}$ of PI (Fig. S5 d-i). This shows that finding at least as many regions that adhere to the WWDD paradigm

by chance is highly unlikely ($p < 0.01$ in all cases). In contrast, the fraction of ΔMDyn-dominated regions, which fulfill WWDD for 4xCO$_2$ or DWWD for the LGM, is not statistically significant. Thus, we conclude that there is indeed a robust preference for thermodynamic dominated regions to obey the WWDD (DWWD) paradigm.

Finally, we test the importance of the thermodynamic scaling components for the WWDD paradigm in regions with thermodynamic domination. As the thermodynamic domination by ΔMTh only considers the mean flow and neglects transient eddies, we restrict the analysis to the mean flow component of the thermodynamic scaling (Eq. 15). As expected from the derivation of the WWDD paradigm, all thermodynamically dominated regions, for which the local temperature term has a dominant influence in the thermodynamic scaling, obey WWDD for 4xCO$_2$ and DWWD for the LGM. Taking a closer look at the ΔMTh dominated regions without a decisive contribution by the local temperature term, we find that 15 of 17 still obey WWDD for 4xCO$_2$ and 6 of 7 still obey DWWD for the LGM. Thus, having a dominant thermodynamic contribution seems to be a very good indicator for adhering to the WWDD paradigm even if there is no dominant contribution by the local temperature term.

Beyond analyzing the signs of $P - E$ changes, we compare the amplitudes of $P - E$ during PI and $\Delta(P - E)$. For better comparability, we rescale $\Delta(P - E)$ by the local temperature change and the Clausius-Clapeyron scaling coefficient α. When we consider all regions or just the regions without dominant thermodynamic contribution to ΔMEAN, $P - E$ during PI has very little predictive power for LGM and 4xCO$_2$ changes as quantified by the explained variance r^2 (Fig. 10). In contrast, we find higher r^2 values for regions with dominant thermodynamic contributions to ΔMEAN, in particular for 4xCO$_2$. On average, $\Delta(P - E)$ follows the simple scaling in these regions as indicated by slopes close to 1 in Fig. 10c,d. This suggests that the sign in thermodynamically dominated regions is primarily determined by the local temperature term, whereas the sum of all other contributions leads to random deviations from the simple thermodynamic scaling relationship which, in most cases, do not change the sign of $\Delta(P - E)$.

5 Discussion

Our results show a strong state dependency of the patterns and varying importance of the moisture budget contributions. However, we also detect robust relationships across states such as the proportion of mean flow versus transient eddy contributions, the relative importance of the thermodynamic scaling terms, the strong adherence to the WWDD paradigm for thermodynamically dominated regions, and the closed global budgets for the individual moisture budget contributions.

In the following, we first discuss whether and how the spatial structure of the radiative forcing could explain the state dependency of moisture budget contributions. Then, we deduce limitations for the LGM as a cold world analog for future hydroclimate changes. Finally, we suggest potential mechanisms that could explain the state invariant relationships found in our analysis.

5.1 Dependence of moisture budget contributions on spatial structure of the forcings

We find substantial differences in the patterns and relative importance of the moisture budget contributions for the three climate states. In particular, dynamic changes are the most relevant for the midH and the least important for 4xCO$_2$, the correlation of LGM and 4xCO$_2$ ΔMDyn patterns is insignificant, and the dynamic and thermodynamic changes oppose each other for 4xCO$_2$ and for the midH over land, but not the LGM and the midH over oceans (Sect. 4.2). We attribute the diagnosed differences between the states mainly to the different spatial and potentially seasonal structure of the boundary condition changes, in accordance with previous studies (e.g., D'Agostino et al., 2019, 2020; Lora, 2018; Lowry and Morrill, 2019; McGee, 2020). For 4xCO$_2$, only CO$_2$ concentrations are changed, while the biggest contributions to the LGM forcing come from GHG and ice sheet changes, and the midH differs from the PI mostly by an altered orbital parameter configuration.

Our results suggest that the spatially homogeneous GHG forcing leads to zonally homogeneous and hemispherically symmetric changes. In the analyzed 4xCO$_2$ simulation, the symmetric structure in
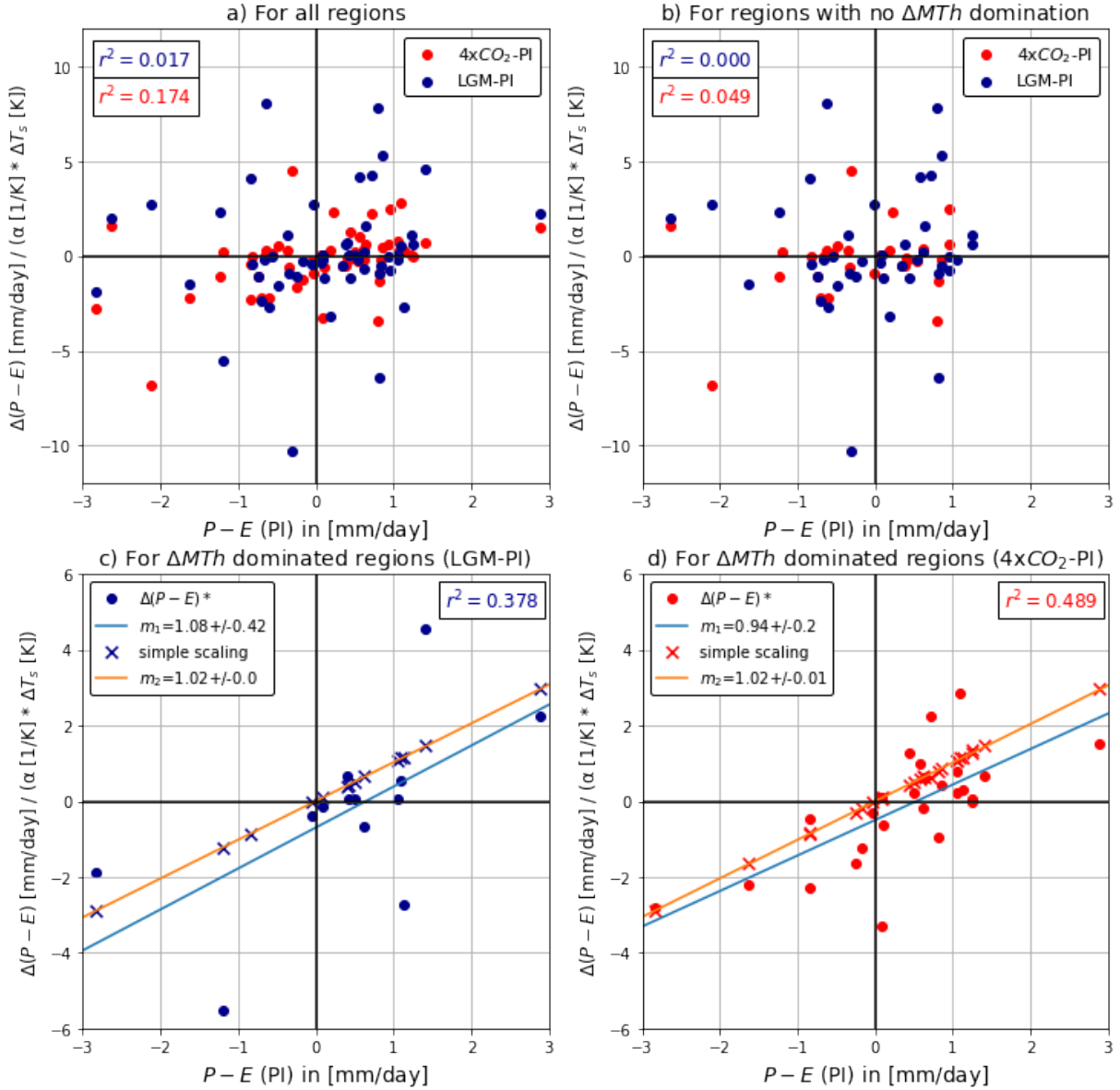
Figure 10: (a) Comparison of regional mean annual mean $P-E$ during PI with LGM and 4xCO$_2$ $\Delta(P-E)^*$, rescaled by the local temperature change and α. The rescaling makes regions with different magnitudes of temperature changes comparable. (b) Same as (a) but restricted to regions without dominant thermodynamic contributions to ΔMEAN. (c-d) Same as (b) but for regions with dominant thermodynamic contribution to ΔMEAN for (c) the LGM and (d) 4xCO$_2$. The strength of the linear relationship between $P-E$(PI) and rescaled $\Delta(P-E)^*$, quantified by the squared correlation r^2, is given in the top right of each panel. In (c) and (d), we also show the slopes of a linear fit. The simple scaling alone would lead to a perfect 1-to-1 relationship. Note that we removed two outlier regions for the LGM that resulted from dividing by very small temperature changes (South Australia with dominant thermodynamic and South Asia with dominant dynamic contribution to ΔMEAN).

the inner tropics originates from a combination of thermodynamic changes, which accentuate the PI pattern, and dynamic changes, perhaps driven by differences in the spatial structure of mass flux convergence (Chadwick et al., 2013). Moreover, the homogeneous structure of GHG forcing results in smaller contributions from circulation than specific humidity changes such that the number of thermodynamically dominated regions is almost twice as high as the amount of dynamically dominated regions (Sect. 4.2). In contrast, the dynamically dominated regions outnumber the thermodynamically dominated regions for the LGM. We attribute this difference to the stronger effects of ice sheet forcing on circulation. While the ice sheet forcing leads to major changes in specific humidity at the locations of the Laurentide, Fennoscandian, and Patagonian ice sheets, it has global impacts on the circulation, which tend to be zonally inhomogeneous and hemispherically asymmetric.

The higher importance of the dynamic term for the midH than for the LGM and $4xCO_2$ is likely due to the relatively small changes in GHG forcing compared to orbital forcing. The latter is hemispherically asymmetric and varies seasonally. This manifests in major circulation changes in the tropics and subtropics but relatively minor changes in the extratropics. A zonally more homogeneous structure of the dynamic term in the midH compared to the LGM can be attributed to the zonal homogeneity of orbital forcing. The deduced spatial structures of $P - E$ changes due to GHG, ice sheet, and orbital forcing in the MPI-ESM simulations are mostly in agreement with LGM sensitivity experiments by Shi et al. (2023). Our analysis does not quantify to what extent local forcing effects, atmospheric teleconnections, and feedback processes such as cloud and climate-vegetation feedbacks contribute to the different moisture budget terms. Sensitivity simulations to isolate the impacts of specific processes could provide further insights into the local and remote influences of the different forcings.

Our results have implications for the LGM as a potential hydroclimate cold world analog to a warm future (Quade and Broecker, 2009). Previous studies showed that on the global scale and for zonal means, WWDD tends to be satisfied under future emission scenarios (e.g., Chou et al., 2009; Held and Soden, 2006; Polson et al., 2013; Roderick et al., 2014). Additionally, multi-model mean analyses for the LGM found zonal mean drying over the tropics and high latitudes, and zonal mean wetting over the mid-latitudes (e.g., Boos, 2012; Rehfeld et al., 2020), which indicates a reverse pattern to the future scenarios. In our analysis, only the thermodynamic term is subject to a strong anticorrelation between LGM and $4xCO_2$, and the locations with dominant thermodynamic contributions vary substantially between LGM and $4xCO_2$ (Sect. 4.2). The regionally-dependent applicability of the LGM as a cold world analog in our study is in agreement with a model-data comparison study for North and South America by Lowry and Morrill (2019) and a multi-model study by Boos (2012), who found a limited applicability of thermodynamic scalings for the LGM. Both of these studies argue in particular with the importance of dynamic processes for the LGM and also the role of the LGM ice sheets on thermodynamically driven changes. Similar to the suggested limitations in transferring model skill for the LGM to projected future $P - E$ changes, our results indicate that accurate modeling of midH $P - E$ does not directly transfer to future projections due to the varying importance of dynamic and thermodynamic contributions.

5.2 State-invariant relationships between contributions

Despite the strong state dependency of moisture budget contributions, we find robust relationships among and between contributions across states. We tentatively attribute these to two reasons. On the one hand, local processes, which are barely affected by the changing boundary conditions, could control the relationship. On the other hand, they could result from a strong influence from boundary conditions which undergo only minor changes, such as land-sea masks and meridional insolation gradients. For example, there is a consistent anticorrelation between the temperature and relative humidity gradient terms in the thermodynamic scaling across all three states (Sect. 4.3). We propose that this anticorrelation is related to localized climate change, particularly over land where gradients are largest. For example, precipitation, evaporation, and relative humidity tend to increase over the same land areas, particularly for the LGM and midH (not shown). In turn, this can cool the surface through increased cloud cover and latent heat fluxes.

Unlike the thermodynamic and dynamic contributions to the moisture budget, the relative importance

patterns of the thermodynamic scaling terms vary little between states. While the local temperature term has a higher relative importance over ocean than land, the spatial gradient terms, especially that of relative humidity, are consistently more important over land than ocean (Sect. 4.3). We attribute this to the heterogeneous water supply from land surfaces that leads to a more regionalized relative humidity response to global warming over land than ocean. Furthermore, the areas with the strongest temperature and relative humidity gradient contributions are also the areas with the largest absolute gradients for PI, subtropical land areas for relative humidity, and the mid-latitudes for temperature. The position of these areas is mainly controlled by the global atmospheric circulation, which is strongly constrained by boundary conditions that change only little between the three considered states, such as meridional insolation gradients, land-sea masks, and topography.

While our results support previous evidence for a limited applicability of the WWDD paradigm on the regional scale (e.g., Byrne and O'Gorman, 2015; Chadwick et al., 2013; Greve et al., 2014; Li et al., 2021), we find a highly predictive precondition for WWDD to hold, independent of the state and whether a region is covered by land or ocean. Namely, we show that thermodynamically dominated regions are highly likely to obey WWDD for $4xCO_2$ and DWWD for the LGM, while dynamically dominated regions adhere to the WWDD paradigm roughly as often as expected by chance (Sect. 4.4). Thus, the global-scale applicability of the paradigm depends on the importance of thermodynamic contributions. This implies in particular a better applicability of the paradigm for future scenarios than for paleoclimate states. Further investigation of the different thermodynamic contributions reveals that a dominant influence of the local temperature term, which was used to derive the WWDD paradigm (Held and Soden, 2006), is not a decisive condition for WWDD to hold. We are not aware of general mechanisms that explain why terms in the thermodynamic scaling besides the local temperature term would favor $P - E$ changes following the WWDD concept. This suggests that at least in regions with a dominant thermodynamic contribution but without a dominant local temperature term, compensating effects between the other moisture budget contributions appear relevant. Specifically, the sum of all other contributions tend to not switch the sign of $P - E$ changes prescribed by the simple thermodynamic scaling in these regions.

Finally, the individual moisture budget terms do not only all vanish in the global mean, but they also converge towards a closed budget with similar rates of decay (Sect. 4.2). This result extends the large-scale constraint for $\Delta(P - E)$ demonstrated by Dagan et al. (2019). The similarity of the rates of decay despite strongly varying radiative forcing patterns suggests that the decay is mainly governed by physical processes that are independent of the specific forcing. In particular, the strength and spatial patterns of the forcing seem to determine the total spatial variability of moisture budget contributions but not the decay towards a closed budget. Dependencies between local temperature changes, temperature gradient changes, and circulation changes driven by the changing local energy budget seem to lead to a similar spatial scale of thermodynamic and dynamic processes. Testing the general applicability of the rates of decay, derived here for MPI-ESM simulations, requires a comparison with other models and reanalysis data. This can facilitate the exploitation of our results for deriving large-scale tendencies, which could complement existing theoretical constraints for the hydrological cycle (e.g., Allen and Ingram, 2002; Dagan and Stier, 2020; Muller and O'Gorman, 2011; O'Gorman et al., 2012).

6 Conclusions

In this study, we examine the state dependency of thermodynamic, dynamic, and transient eddy contributions to effective precipitation ($P - E$) changes for the Last Glacial Maximum (LGM), the mid-Holocene (midH), and abrupt quadrupling of CO_2 concentrations ($4xCO_2$) using CMIP6/PMIP4 simulations from MPI-ESM1.2-LR. We find a strong influence of the spatial structure of the radiative forcing on the regional and global importance of thermodynamic compared to dynamic contributions to $P - E$ changes, and the patterns associated with the dynamic contributions. In contrast, the importance of mean flow compared to transient eddy contributions is relatively consistent across states.

We attribute hemispherically more asymmetric and zonally more heterogeneous dynamic contributions for the LGM compared to 4xCO$_2$ to the global-scale influence of the LGM ice sheet forcing on the atmospheric circulation. The additionally much larger importance of dynamic contributions for the LGM and midH compared to 4xCO$_2$ limits the transferability of results on hydroclimate changes during these periods to scenarios for the next centuries. This is because the latter are dominated by changes in greenhouse gas concentrations which favor thermodynamically driven $P - E$ changes.

However, we also find consistent relationships across climate states. The wet-get-wetter-dry-get-drier (WWDD) paradigm holds for almost all regions dominated by thermodynamic contributions, independent of whether a region is covered by land or ocean and of the importance of the local temperature term, for which the paradigm holds by definition. However for regions dominated by dynamic contributions, WWDD patterns do not occur more often than expected by chance. Additionally, the spatial patterns of the importance of the thermodynamic scaling terms are consistent across states, with the highest importance of the local temperature term in the tropics and high latitudes, the temperature gradient term in the mid-latitudes, and the relative humidity gradient term in land areas with low precipitation amounts. We attribute this to the dominating role of stable features across states such as meridional insolation gradients and land-sea masks.

Finally, we find that the individual contributions to the moisture budget vanish in the global mean. Moreover, their spatial variability decays with similar rates for increasing spatial scales. In contrast, the terms of the thermodynamic scaling do not vanish in the global mean. This means that compensating effects between local and spatial gradient terms are needed to close the global moisture budget, but not the interaction between thermodynamic and dynamic changes. Our study focuses on one model to ensure that differences between states are indeed the result of boundary condition changes and not of different model configurations. We encourage testing the robustness of our results for more models and climate states in future research, in particular past warm climates (e.g., Burls et al., 2021; Haywood et al., 2020).

Acknowledgments

Data availability statement

The MPI-ESM1.2-LR simulation output was downloaded from the Earth System Grid Federation (ESGF) node at DKRZ: https://esgf-data.dkrz.de/search/cmip6-dkrz/ (Last Accessed: 30.04.2024). The simulations can be accessed through Jungclaus et al. (2019a,b); Wieners et al. (2019b,a). Code to reproduce our analysis is archived on zenodo (Braschoss et al., 2024).

7 References

Adam, M., Weitzel, N., and Rehfeld, K.: Identifying Global-Scale Patterns of Vegetation Change During the Last Deglaciation From Paleoclimate Networks, Paleoceanogr Paleoclimatol, 36, e2021PA004 265, https://doi.org/10.1029/2021PA004265, 2021.

Allan, R. P., Barlow, M., Byrne, M. P., Cherchi, A., Douville, H., Fowler, H. J., Gan, T. Y., Pendergrass, A. G., Rosenfeld, D., Swann, A. L. S., Wilcox, L. J., and Zolina, O.: Advances in understanding large-scale responses of the water cycle to climate change, Ann. N.Y. Acad. Sci., 1472, 49–75, https://doi.org/10.1111/nyas.14337, 2020.

Allen, M. R. and Ingram, W. J.: Constraints on future changes in climate and the hydrologic cycle, Nature, 419, 228–232, https://doi.org/10.1038/nature01092, 2002.

Argus, D. F., Peltier, W. R., Drummond, R., and Moore, A. W.: The Antarctica component of postglacial rebound model ICE-6G_C (VM5a) based on GPS positioning, exposure age dating of ice thicknesses, and relative sea level histories, Geophysical Journal International, 198, 537–563, https://doi.org/10.1093/gji/ggu140, 2014.

Armstrong, E., Izumi, K., and Valdes, P.: Identifying the mechanisms of DO-scale oscillations in a GCM: a salt oscillator triggered by the Laurentide ice sheet, Clim Dyn, 60, 3983–4001, https://doi.org/10.1007/s00382-022-06564-y, 2023.

Bereiter, B., Eggleston, S., Schmitt, J., Nehrbass-Ahles, C., Stocker, T. F., Fischer, H., Kipfstuhl, S., and Chappellaz, J.: Revision of the EPICA Dome C CO_2 record from 800 to 600 kyr before present, Geophys. Res. Lett., 42, 542–549, https://doi.org/10.1002/2014GL061957, 2015.

Berger, A.: Long-Term Variations of Daily Insolation and Quaternary Climatic Changes, J. Atmos. Sci., 35, 2362–2367, https://doi.org/10.1175/1520-0469(1978)035⟨2362:LTVODI⟩2.0.CO;2, 1978.

Boos, W. R.: Thermodynamic Scaling of the Hydrological Cycle of the Last Glacial Maximum, J. Climate, 25, 992–1006, https://doi.org/10.1175/JCLI-D-11-00010.1, 2012.

Braschoss, L., Weitzel, N., Baudouin, J.-P., and Rehfeld, K.: Code for "State-dependency of dynamic and thermodynamic contributions to effective precipitation changes", https://doi.org/10.5281/zenodo.11572566, 2024.

Brierley, C. M., Zhao, A., Harrison, S. P., Braconnot, P., Williams, C. J. R., Thornalley, D. J. R., Shi, X., Peterschmitt, J.-Y., Ohgaito, R., Kaufman, D. S., Kageyama, M., Hargreaves, J. C., Erb, M. P., Emile-Geay, J., D'Agostino, R., Chandan, D., Carré, M., Bartlein, P. J., Zheng, W., Zhang, Z., Zhang, Q., Yang, H., Volodin, E. M., Tomas, R. A., Routson, C., Peltier, W. R., Otto-Bliesner, B., Morozova, P. A., McKay, N. P., Lohmann, G., Legrande, A. N., Guo, C., Cao, J., Brady, E., Annan, J. D., and Abe-Ouchi, A.: Large-scale features and evaluation of the PMIP4-CMIP6 midHolocene simulations, Clim. Past, 16, 1847–1872, https://doi.org/10.5194/cp-16-1847-2020, 2020.

Burls, N. J., Bradshaw, C. D., De Boer, A. M., Herold, N., Huber, M., Pound, M., Donnadieu, Y., Farnsworth, A., Frigola, A., Gasson, E., Von Der Heydt, A. S., Hutchinson, D. K., Knorr, G., Lawrence, K. T., Lear, C. H., Li, X., Lohmann, G., Lunt, D. J., Marzocchi, A., Prange, M., Riihimaki, C. A., Sarr, A., Siler, N., and Zhang, Z.: Simulating Miocene Warmth: Insights From an Opportunistic Multi-Model Ensemble (MioMIP1), Paleoceanogr Paleoclimatol, 36, https://doi.org/10.1029/2020PA004054, 2021.

Byrne, M. P. and O'Gorman, P. A.: The Response of Precipitation Minus Evapotranspiration to Climate Warming: Why the "Wet-Get-Wetter, Dry-Get-Drier" Scaling Does Not Hold over Land, J. Climate, 28, 8078–8092, https://doi.org/10.1175/JCLI-D-15-0369.1, 2015.

Chadwick, R., Boutle, I., and Martin, G.: Spatial Patterns of Precipitation Change in CMIP5: Why the Rich Do Not Get Richer in the Tropics, J. Climate, 26, 3803–3822, https://doi.org/10.1175/JCLI-D-12-00543.1, 2013.

Chou, C., Neelin, J. D., Chen, C.-A., and Tu, J.-Y.: Evaluating the "Rich-Get-Richer" Mechanism in Tropical Precipitation Change under Global Warming, J. Climate, 22, 1982–2005, https://doi.org/10.1175/2008JCLI2471.1, 2009.

Dagan, G. and Stier, P.: Constraint on precipitation response to climate change by combination of atmospheric energy and water budgets, npj Clim Atmos Sci, 3, 1–5, https://doi.org/10.1038/s41612-020-00137-8, 2020.

Dagan, G., Stier, P., and Watson-Parris, D.: Analysis of the Atmospheric Water Budget for Elucidating the Spatial Scale of Precipitation Changes Under Climate Change, Geophys. Res. Lett., 46, 10 504–10 511, https://doi.org/10.1029/2019GL084173, 2019.

D'Agostino, R., Lionello, P., Adam, O., and Schneider, T.: Factors controlling Hadley circulation changes from the Last Glacial Maximum to the end of the 21st century, Geophys. Res. Lett., 44, 8585–8591, https://doi.org/10.1002/2017GL074533, 2017.

D'Agostino, R., Bader, J., Bordoni, S., Ferreira, D., and Jungclaus, J.: Northern Hemisphere Monsoon Response to Mid-Holocene Orbital Forcing and Greenhouse Gas-Induced Global Warming, Geophys. Res. Lett., 46, 1591–1601, https://doi.org/10.1029/2018GL081589, 2019.

D'Agostino, R., Brown, J. R., Moise, A., Nguyen, H., Dias, P. L. S., and Jungclaus, J.: Contrasting Southern Hemisphere Monsoon Response: MidHolocene Orbital Forcing versus Future Greenhouse Gas–Induced Global Warming, J. Climate, 33, 9595–9613, https://doi.org/10.1175/JCLI-D-19-0672.1, 2020.

Di Cecco, G. J. and Gouhier, T. C.: Increased spatial and temporal autocorrelation of temperature under climate change, Sci Rep, 8, 14 850, https://doi.org/10.1038/s41598-018-33217-0, 2018.

Douville, H., Raghavan, K., Renwick, J., Allan, R. P., Arias, P. A., Barlow, M., Cerezo-Mota, R., Cherchi, A., Gan, T. Y., Gergis, J., Jiang, D., Khan, A., Mba, W. P., Rosenfeld, D., Tierney, J., and Zolina, O.: Water cycle changes, in: Climate Change 2021: The Physical Science Basis. Contribution of Working Group I to the Sixth Assessment Report of the Intergovernmental Panel on Climate Change, edited by Masson-Delmotte, V. P., Zhai, P., Pirani, A., Connors, S. L., Péan, C., Berger, S., Caud, N., Chen, Y., Goldfarb, L., Gomis, M. I., Huang, M., Leitzell, K., Lonno, E., Matthews, J. B. R., Maycock, T. K., Waterfield, T., Yelekçi, O., Yu, R., and Zhou, B., pp. 1055–1210, Cambridge University Press, Cambridge, United Kingdom and New York, NY, USA, https://doi.org/10.1017/9781009157896.010, 2021.

Elbaum, E., Garfinkel, C. I., Adam, O., Morin, E., Rostkier-Edelstein, D., and Dayan, U.: Uncertainty in Projected Changes in Precipitation Minus Evaporation: Dominant Role of Dynamic Circulation Changes and Weak Role for Thermodynamic Changes, Geophys. Res. Lett., 49, https://doi.org/10.1029/2022GL097725, 2022.

Eyring, V., Bony, S., Meehl, G. A., Senior, C. A., Stevens, B., Stouffer, R. J., and Taylor, K. E.: Overview of the Coupled Model Intercomparison Project Phase 6 (CMIP6) experimental design and organization, Geosci. Model Dev., 9, 1937–1958, https://doi.org/10.5194/gmd-9-1937-2016, 2016.

Fu, Q. and Feng, S.: Responses of terrestrial aridity to global warming, J. Geophys. Res. Atmos., 119, 7863–7875, https://doi.org/10.1002/2014JD021608, 2014.

Gimeno-Sotelo, L., Sorí, R., Nieto, R., Vicente-Serrano, S. M., and Gimeno, L.: Unravelling the origin of the atmospheric moisture deficit that leads to droughts, Nat Water, 2, 242–253, https://doi.org/10.1038/s44221-023-00192-4, 2024.

Greve, P., Orlowsky, B., Mueller, B., Sheffield, J., Reichstein, M., and Seneviratne, S. I.: Global assessment of trends in wetting and drying over land, Nature Geosci, 7, 716–721, https://doi.org/10.1038/ngeo2247, 2014.

Haywood, A. M., Tindall, J. C., Dowsett, H. J., Dolan, A. M., Foley, K. M., Hunter, S. J., Hill, D. J., Chan, W.-L., Abe-Ouchi, A., Stepanek, C., Lohmann, G., Chandan, D., Peltier, W. R.,

Tan, N., Contoux, C., Ramstein, G., Li, X., Zhang, Z., Guo, C., Nisancioglu, K. H., Zhang, Q., Li, Q., Kamae, Y., Chandler, M. A., Sohl, L. E., Otto-Bliesner, B. L., Feng, R., Brady, E. C., von der Heydt, A. S., Baatsen, M. L. J., and Lunt, D. J.: The Pliocene Model Intercomparison Project Phase 2: large-scale climate features and climate sensitivity, Clim. Past, 16, 2095–2123, https://doi.org/10.5194/cp-16-2095-2020, 2020.

Held, I. M. and Soden, B. J.: Robust Responses of the Hydrological Cycle to Global Warming, J. Climate, 19, 5686–5699, https://doi.org/10.1175/JCLI3990.1, 2006.

Iturbide, M., Gutiérrez, J. M., Alves, L. M., Bedia, J., Cerezo-Mota, R., Cimadevilla, E., Cofiño, A. S., Di Luca, A., Faria, S. H., Gorodetskaya, I. V., Hauser, M., Herrera, S., Hennessy, K., Hewitt, H. T., Jones, R. G., Krakovska, S., Manzanas, R., Martínez-Castro, D., Narisma, G. T., Nurhati, I. S., Pinto, I., Seneviratne, S. I., van den Hurk, B., and Vera, C. S.: An update of IPCC climate reference regions for subcontinental analysis of climate model data: definition and aggregated datasets, Earth Syst. Sci. Data, 12, 2959–2970, https://doi.org/10.5194/essd-12-2959-2020, 2020.

Jiang, W., Gastineau, G., and Codron, F.: Multicentennial Variability Driven by Salinity Exchanges Between the Atlantic and the Arctic Ocean in a Coupled Climate Model, J Adv Model Earth Syst, 13, e2020MS002 366, https://doi.org/10.1029/2020MS002366, 2021.

Jungclaus, J., Mikolajewicz, U., Kapsch, M.-L., D'Agostino, R., Wieners, K.-H., Giorgetta, M., Reick, C., Esch, M., Bittner, M., Legutke, S., Schupfner, M., Wachsmann, F., Gayler, V., Haak, H., de Vrese, P., Raddatz, T., Mauritsen, T., von Storch, J.-S., Behrens, J., Brovkin, V., Claussen, M., Crueger, T., Fast, I., Fiedler, S., Hagemann, S., Hohenegger, C., Jahns, T., Kloster, S., Kinne, S., Lasslop, G., Kornblueh, L., Marotzke, J., Matei, D., Meraner, K., Modali, K., Müller, W., Nabel, J., Notz, D., Peters-von Gehlen, K., Pincus, R., Pohlmann, H., Pongratz, J., Rast, S., Schmidt, H., Schnur, R., Schulzweida, U., Six, K., Stevens, B., Voigt, A., and Roeckner, E.: MPI-M MPI-ESM1.2-LR model output prepared for CMIP6 PMIP lgm, https://doi.org/10.22033/ESGF/CMIP6.6642, 2019a.

Jungclaus, J., Mikolajewicz, U., Kapsch, M.-L., D'Agostino, R., Wieners, K.-H., Giorgetta, M., Reick, C., Esch, M., Bittner, M., Legutke, S., Schupfner, M., Wachsmann, F., Gayler, V., Haak, H., de Vrese, P., Raddatz, T., Mauritsen, T., von Storch, J.-S., Behrens, J., Brovkin, V., Claussen, M., Crueger, T., Fast, I., Fiedler, S., Hagemann, S., Hohenegger, C., Jahns, T., Kloster, S., Kinne, S., Lasslop, G., Kornblueh, L., Marotzke, J., Matei, D., Meraner, K., Modali, K., Müller, W., Nabel, J., Notz, D., Peters-von Gehlen, K., Pincus, R., Pohlmann, H., Pongratz, J., Rast, S., Schmidt, H., Schnur, R., Schulzweida, U., Six, K., Stevens, B., Voigt, A., and Roeckner, E.: MPI-M MPI-ESM1.2-LR model output prepared for CMIP6 PMIP midHolocene, https://doi.org/10.22033/ESGF/CMIP6.6644, 2019b.

Kageyama, M., Albani, S., Braconnot, P., Harrison, S. P., Hopcroft, P. O., Ivanovic, R. F., Lambert, F., Marti, O., Peltier, W. R., Peterschmitt, J.-Y., Roche, D. M., Tarasov, L., Zhang, X., Brady, E. C., Haywood, A. M., LeGrande, A. N., Lunt, D. J., Mahowald, N. M., Mikolajewicz, U., Nisancioglu, K. H., Otto-Bliesner, B. L., Renssen, H., Tomas, R. A., Zhang, Q., Abe-Ouchi, A., Bartlein, P. J., Cao, J., Li, Q., Lohmann, G., Ohgaito, R., Shi, X., Volodin, E., Yoshida, K., Zhang, X., and Zheng, W.: The PMIP4 contribution to CMIP6 – Part 4: Scientific objectives and experimental design of the PMIP4-CMIP6 Last Glacial Maximum experiments and PMIP4 sensitivity experiments, Geosci. Model Dev., 10, 4035–4055, https://doi.org/10.5194/gmd-10-4035-2017, 2017.

Kageyama, M., Braconnot, P., Harrison, S. P., Haywood, A. M., Jungclaus, J. H., Otto-Bliesner, B. L., Peterschmitt, J.-Y., Abe-Ouchi, A., Albani, S., Bartlein, P. J., Brierley, C., Crucifix, M., Dolan, A., Fernandez-Donado, L., Fischer, H., Hopcroft, P. O., Ivanovic, R. F., Lambert, F., Lunt, D. J., Mahowald, N. M., Peltier, W. R., Phipps, S. J., Roche, D. M., Schmidt, G. A., Tarasov, L., Valdes, P. J., Zhang, Q., and Zhou, T.: The PMIP4 contribution to CMIP6 – Part 1: Overview and over-arching analysis plan, Geosci. Model Dev., 11, 1033–1057, https://doi.org/10.5194/gmd-11-1033-2018, 2018.

Kageyama, M., Harrison, S. P., Kapsch, M.-L., Lofverstrom, M., Lora, J. M., Mikolajewicz, U., Sherriff-Tadano, S., Vadsaria, T., Abe-Ouchi, A., Bouttes, N., Chandan, D., Gregoire, L. J., Ivanovic, R. F., Izumi, K., LeGrande, A. N., Lhardy, F., Lohmann, G., Morozova, P. A., Ohgaito, R., Paul, A., Peltier, W. R., Poulsen, C. J., Quiquet, A., Roche, D. M., Shi, X., Tierney, J. E., Valdes, P. J., Volodin, E., and Zhu, J.: The PMIP4 Last Glacial Maximum experiments: preliminary results and comparison with the PMIP3 simulations, Clim. Past, 17, 1065–1089, https://doi.org/10.5194/cp-17-1065-2021, 2021.

Lakhankar, T., Jones, A. S., Combs, C. L., Sengupta, M., Vonder Haar, T. H., and Khanbilvardi, R.: Analysis of Large Scale Spatial Variability of Soil Moisture Using a Geostatistical Method, Sensors, 10, 913–932, https://doi.org/10.3390/s100100913, 2010.

Li, G., Si, M., Zhang, C., Shen, Z., Wang, S., and Shao, J.: Responses of plant biomass and biomass allocation to experimental drought: A global phylogenetic meta-analysis, Agricultural and Forest Meteorology, 347, 109 917, https://doi.org/10.1016/j.agrformet.2024.109917, 2024.

Li, Y., Zhang, Y., Ye, W., and Zhang, X.: Global Wet/Dry Patterns and Mechanisms Since the Last Glacial Maximum: A Key to Future Projection, Earth's Future, 9, https://doi.org/10.1029/2020EF001907, 2021.

Liu, C. and Allan, R. P.: Observed and simulated precipitation responses in wet and dry regions 1850–2100, Environ. Res. Lett., 8, 034 002, https://doi.org/10.1088/1748-9326/8/3/034002, 2013.

Lora, J. M.: Components and Mechanisms of Hydrologic Cycle Changes over North America at the Last Glacial Maximum, J. Climate, 31, 7035–7051, https://doi.org/10.1175/JCLI-D-17-0544.1, 2018.

Lowry, D. P. and Morrill, C.: Is the Last Glacial Maximum a reverse analog for future hydroclimate changes in the Americas?, Clim Dyn, 52, 4407–4427, https://doi.org/10.1007/s00382-018-4385-y, 2019.

Mauritsen, T., Bader, J., Becker, T., Behrens, J., Bittner, M., Brokopf, R., Brovkin, V., Claussen, M., Crueger, T., Esch, M., Fast, I., Fiedler, S., Fläschner, D., Gayler, V., Giorgetta, M., Goll, D. S., Haak, H., Hagemann, S., Hedemann, C., Hohenegger, C., Ilyina, T., Jahns, T., Jimenéz-de-la-Cuesta, D., Jungclaus, J., Kleinen, T., Kloster, S., Kracher, D., Kinne, S., Kleberg, D., Lasslop, G., Kornblueh, L., Marotzke, J., Matei, D., Meraner, K., Mikolajewicz, U., Modali, K., Möbis, B., Müller, W. A., Nabel, J. E. M. S., Nam, C. C. W., Notz, D., Nyawira, S., Paulsen, H., Peters, K., Pincus, R., Pohlmann, H., Pongratz, J., Popp, M., Raddatz, T. J., Rast, S., Redler, R., Reick, C. H., Rohrschneider, T., Schemann, V., Schmidt, H., Schnur, R., Schulzweida, U., Six, K. D., Stein, L., Stemmler, I., Stevens, B., Storch, J., Tian, F., Voigt, A., Vrese, P., Wieners, K., Wilkenskjeld, S., Winkler, A., and Roeckner, E.: Developments in the MPI-M Earth System Model version 1.2 (MPI-ESM1.2) and Its Response to Increasing CO_2, J. Adv. Model. Earth Syst., 11, 998–1038, https://doi.org/10.1029/2018MS001400, 2019.

McGee, D.: Glacial–Interglacial Precipitation Changes, Annu. Rev. Mar. Sci., 12, 525–557, https://doi.org/10.1146/annurev-marine-010419-010859, 2020.

Mehling, O., Bellomo, K., Angeloni, M., Pasquero, C., and Von Hardenberg, J.: High-latitude precipitation as a driver of multicentennial variability of the AMOC in a climate model of intermediate complexity, Clim Dyn, 61, 1519–1534, https://doi.org/10.1007/s00382-022-06640-3, 2023.

Muller, C. J. and O'Gorman, P. A.: An energetic perspective on the regional response of precipitation to climate change, Nature Clim Change, 1, 266–271, https://doi.org/10.1038/nclimate1169, 2011.

Otto-Bliesner, B. L., Braconnot, P., Harrison, S. P., Lunt, D. J., Abe-Ouchi, A., Albani, S., Bartlein, P. J., Capron, E., Carlson, A. E., Dutton, A., Fischer, H., Goelzer, H., Govin, A., Haywood, A., Joos, F., LeGrande, A. N., Lipscomb, W. H., Lohmann, G., Mahowald, N., Nehrbass-Ahles, C.,

Pausata, F. S. R., Peterschmitt, J.-Y., Phipps, S. J., Renssen, H., and Zhang, Q.: The PMIP4 contribution to CMIP6 – Part 2: Two interglacials, scientific objective and experimental design for Holocene and Last Interglacial simulations, Geosci. Model Dev., 10, 3979–4003, https://doi.org/10.5194/gmd-10-3979-2017, 2017.

845 O'Gorman, P. A., Allan, R. P., Byrne, M. P., and Previdi, M.: Energetic Constraints on Precipitation Under Climate Change, Surv Geophys, 33, 585–608, https://doi.org/10.1007/s10712-011-9159-6, 2012.

Peltier, W. R., Argus, D. F., and Drummond, R.: Space geodesy constrains ice age terminal deglaciation: The global ICE-6G_C (VM5a) model, J. Geophys. Res. Solid Earth, 120, 450–487, 850 https://doi.org/10.1002/2014JB011176, 2015.

Polson, D., Hegerl, G. C., Allan, R. P., and Sarojini, B. B.: Have greenhouse gases intensified the contrast between wet and dry regions?, Geophys. Res. Lett., 40, 4783–4787, https://doi.org/10.1002/grl.50923, 2013.

Quade, J. and Broecker, W.: Dryland hydrology in a warmer world: Lessons from the Last Glacial 855 period, Eur. Phys. J. Spec. Top., 176, 21–36, https://doi.org/10.1140/epjst/e2009-01146-y, 2009.

Rehfeld, K., Hébert, R., Lora, J. M., Lofverstrom, M., and Brierley, C. M.: Variability of surface climate in simulations of past and future, Earth Syst. Dynam., 11, 447–468, https://doi.org/10.5194/esd-11-447-2020, 2020.

Roderick, M. L., Sun, F., Lim, W. H., and Farquhar, G. D.: A general framework for understanding 860 the response of the water cycle to global warming over land and ocean, Hydrol. Earth Syst. Sci., 18, 1575–1589, https://doi.org/10.5194/hess-18-1575-2014, 2014.

Scheff, J., Seager, R., Liu, H., and Coats, S.: Are Glacials Dry? Consequences for Paleoclimatology and for Greenhouse Warming, J. Climate, 30, 6593–6609, https://doi.org/10.1175/JCLI-D-16-0854.1, 2017.

865 Seager, R. and Henderson, N.: Diagnostic Computation of Moisture Budgets in the ERA-Interim Reanalysis with Reference to Analysis of CMIP-Archived Atmospheric Model Data, J. Climate, 26, 7876–7901, https://doi.org/10.1175/JCLI-D-13-00018.1, 2013.

Seager, R., Naik, N., and Vecchi, G. A.: Thermodynamic and Dynamic Mechanisms for Large-Scale Changes in the Hydrological Cycle in Response to Global Warming, J. Climate, 23, 4651–4668, 870 https://doi.org/10.1175/2010JCLI3655.1, 2010.

Shi, X., Werner, M., Yang, H., D'Agostino, R., Liu, J., Yang, C., and Lohmann, G.: Unraveling the complexities of the Last Glacial Maximum climate: the role of individual boundary conditions and forcings, Clim. Past, 19, 2157–2175, https://doi.org/10.5194/cp-19-2157-2023, 2023.

Trenberth, K. E. and Guillemot, C. J.: Evaluation of the Global Atmospheric Moisture Budget as 875 Seen from Analyses, J. Climate, 8, 2255–2272, https://doi.org/10.1175/1520-0442(1995)008⟨2255: EOTGAM⟩2.0.CO;2, 1995.

van de Beek, C. Z., Leijnse, H., Torfs, P. J. J. F., and Uijlenhoet, R.: Climatology of daily rainfall semi-variance in The Netherlands, Hydrol. Earth Syst. Sci., 15, 171–183, https://doi.org/10.5194/hess-15-171-2011, 2011.

880 Vicente-Serrano, S. M., Beguería, S., and López-Moreno, J. I.: A Multiscalar Drought Index Sensitive to Global Warming: The Standardized Precipitation Evapotranspiration Index, J. Climate, 23, 1696–1718, https://doi.org/10.1175/2009JCLI2909.1, 2010.

Weij, R., Sniderman, J. M. K., Woodhead, J. D., Hellstrom, J. C., Brown, J. R., Drysdale, R. N., Reed, E., Bourne, S., and Gordon, J.: Elevated Southern Hemisphere moisture availability during glacial periods, Nature, 626, 319–326, https://doi.org/10.1038/s41586-023-06989-3, 2024.

Wieners, K.-H., Giorgetta, M., Jungclaus, J., Reick, C., Esch, M., Bittner, M., Legutke, S., Schupfner, M., Wachsmann, F., Gayler, V., Haak, H., de Vrese, P., Raddatz, T., Mauritsen, T., von Storch, J.-S., Behrens, J., Brovkin, V., Claussen, M., Crueger, T., Fast, I., Fiedler, S., Hagemann, S., Hohenegger, C., Jahns, T., Kloster, S., Kinne, S., Lasslop, G., Kornblueh, L., Marotzke, J., Matei, D., Meraner, K., Mikolajewicz, U., Modali, K., Müller, W., Nabel, J., Notz, D., Peters-von Gehlen, K., Pincus, R., Pohlmann, H., Pongratz, J., Rast, S., Schmidt, H., Schnur, R., Schulzweida, U., Six, K., Stevens, B., Voigt, A., and Roeckner, E.: MPI-M MPI-ESM1.2-LR model output prepared for CMIP6 CMIP piControl, https://doi.org/10.22033/ESGF/CMIP6.6675, 2019a.

Wieners, K.-H., Giorgetta, M., Jungclaus, J., Reick, C., Esch, M., Bittner, M., Legutke, S., Schupfner, M., Wachsmann, F., Gayler, V., Haak, H., de Vrese, P., Raddatz, T., Mauritsen, T., von Storch, J.-S., Behrens, J., Brovkin, V., Claussen, M., Crueger, T., Fast, I., Fiedler, S., Hagemann, S., Hohenegger, C., Jahns, T., Kloster, S., Kinne, S., Lasslop, G., Kornblueh, L., Marotzke, J., Matei, D., Meraner, K., Mikolajewicz, U., Modali, K., Müller, W., Nabel, J., Notz, D., Peters-von Gehlen, K., Pincus, R., Pohlmann, H., Pongratz, J., Rast, S., Schmidt, H., Schnur, R., Schulzweida, U., Six, K., Stevens, B., Voigt, A., and Roeckner, E.: MPI-M MPI-ESM1.2-LR model output prepared for CMIP6 CMIP abrupt-4xCO2, https://doi.org/10.22033/ESGF/CMIP6.6459, 2019b.

Wills, R. C., Byrne, M. P., and Schneider, T.: Thermodynamic and dynamic controls on changes in the zonally anomalous hydrological cycle, Geophys. Res. Lett., 43, 4640–4649, https://doi.org/10.1002/2016GL068418, 2016.

Yang, T., Ding, J., Liu, D., Wang, X., and Wang, T.: Combined Use of Multiple Drought Indices for Global Assessment of Dry Gets Drier and Wet Gets Wetter Paradigm, J. Climate, 32, 737–748, https://doi.org/10.1175/JCLI-D-18-0261.1, 2019.

Zaitchik, B. F., Rodell, M., Biasutti, M., and Seneviratne, S. I.: Wetting and drying trends under climate change, Nat Water, 1, 502–513, https://doi.org/10.1038/s44221-023-00073-w, 2023.

Řehoř, J., Trnka, M., Brázdil, R., Fischer, M., Balek, J., Van Der Schrier, G., and Feng, S.: Global hotspots in soil moisture-based drought trends, Environ. Res. Lett., 19, 014 021, https://doi.org/10.1088/1748-9326/ad0f01, 2024.

Supplement

S1 Introduction

This supplement contains additional plots and tables related to

- the comparison of $\Delta(P-E)^*$ with $\Delta(P-E)$,

- the estimation of effective degrees of freedom for spatial correlations,

- the robustness of regional mean $\Delta(P-E)$ signs,

- the large-scale decay of spatial standard deviations of moisture budget changes,

- the comparison of ΔMTh with the mean circulation part of the thermodynamic scaling,

- and the statistical significance of WWDD / DWWD occurrence.

S2 Comparison of $\Delta(P-E)^*$ with $\Delta(P-E)$ of the simulation

To investigate the limits of the applied moisture budget decomposition, we compare climatological annual mean $\Delta(P-E)$, calculated by directly subtracting the precipitation and evaporation variables, to climatological annual mean $\Delta(P-E)^*$, the sum of all moisture budget decomposition terms. We observe a generally good agreement in both, magnitudes and patterns, between the two terms, but notice some sign disagreements, preferably occurring in regions of particularly low $\Delta(P-E)$ and at high polar latitudes (Fig. S1). Excluding the outermost latitudes that are affected by numerical artefacts from the spatial gradient computation near the poles and applying a 3x3 kernel window smoothing to $\Delta(P-E)$, the area of sign agreement for all three investigated cases is at $\sim 85\%$ of the global area. Applying the smoothing is justified by our interest in the large-scale properties of the moisture budget decomposition terms.
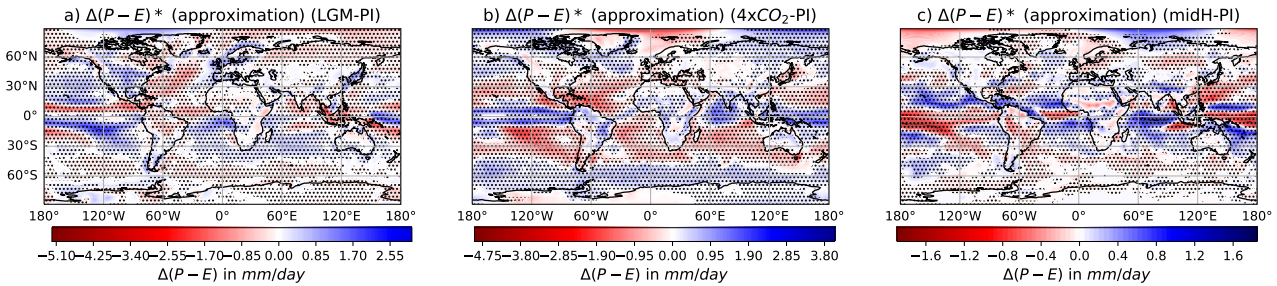

Figure S1: Annual mean $\Delta(P-E)^*$ for (a) the LGM, (b) 4xCO$_2$, and (c) the midH. Stippling indicates sign agreement with smoothed $\Delta(P-E)$ as shown in Fig. 1a-c of the main manuscript.

S3 Semi-variograms for effective degrees of freedom estimation

Fig. S2 shows estimated semi-variograms for the tropics, Northern Hemisphere mid-latitudes, and Southern Hemisphere mid-latitudes. The sill positions in these semi-variograms are used to determine the effective degrees of freedom in our calculation of the confidence intervals for the spatial correlations. The sill position is harder to identify over large regions with high spatial homogeneity (e.g., over the Southern and Arctic Ocean). Therefore, we decided to exclude the high latitude ranges and instead use d^* obtained for the mid-latitudes to estimate the degrees of freedom for the whole extratropics.
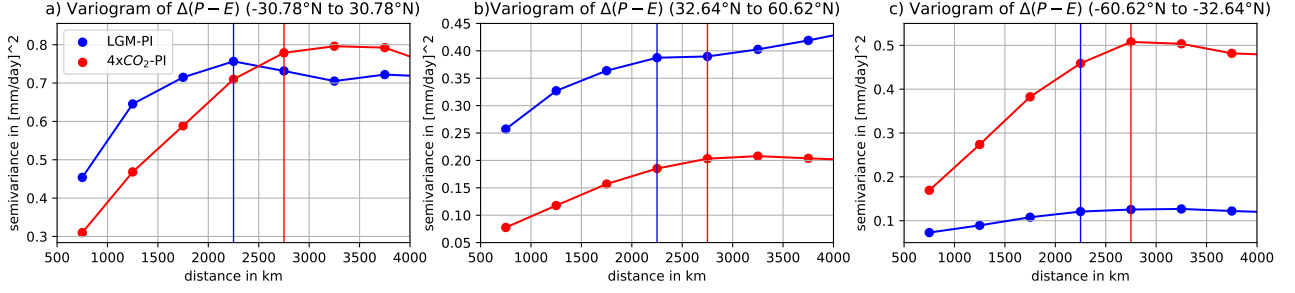
Figure S2: Semi-variograms of annual mean $\Delta(P - E)$ for different latitude ranges, (a) tropics, (b) Northern Hemisphere mid-latitudes, and (c) Southern Hemisphere mid-latitudes. The identified sill positions are marked by vertical lines. The midH values are not shown because of their very small amplitudes.

S4 Robustness of regional $\Delta(P - E)$ signs for the simulation outputs

To test the robustness of the $\Delta(P - E)$ signs, we test for which regions the signs vary when different 30 year intervals are selected in the respective simulations. Regions with changing signs are shown in Fig. S3 for each of the three states.
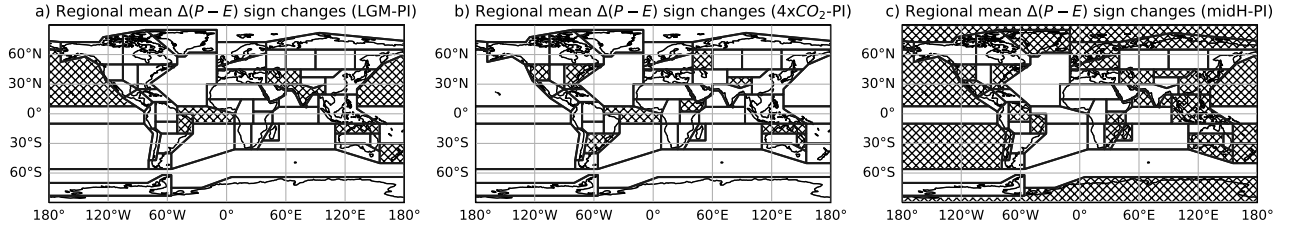

Figure S3: AR6 reference regions that see sign changes in regional mean $\Delta(P - E)$ compared to the alternative 30 year periods (indicated by "x" stippling) for (a) the LGM, (b) 4xCO$_2$, and (c) the midH.

S5 Large-scale decay of spatial standard deviations of moisture budget changes

Here, we provide the estimated global means and exponential decay rates for the six moisture budget terms ΔMTh, $\Delta MDyn$, ΔMNL, ΔMEAN, ΔSME, and $\Delta IntVar$ in each of the three states (Table S1).

Table S1: Global means in [mm/day] and exponential decay rates λ in $[10^{-3}\text{km}^{-1}]$.

	ΔMTh	$\Delta MDyn$	ΔMNL	ΔMEAN	ΔSME	$\Delta IntVar$
Global means [mm day^{-1}]:						
LGM	0.003	0.003	-0.004	0.002	0.02	0.003
4xCO$_2$	-0.004	-0.001	-0.005	-0.009	-0.03	-0.002
midH	0.002	-0.001	-0.002	-0.002	0.004	0.001
Decay rates [10^{-3}km^{-1}]:						
LGM	0.52 ± 0.01	0.59 ± 0.04	0.54 ± 0.04	0.60 ± 0.05	0.63 ± 0.03	0.68 ± 0.04
4xCO$_2$	0.47 ± 0.02	0.64 ± 0.02	0.61 ± 0.04	0.53 ± 0.01	0.61 ± 0.05	0.68 ± 0.05
midH	0.63 ± 0.03	0.66 ± 0.03	0.73 ± 0.05	0.64 ± 0.02	0.71 ± 0.04	0.64 ± 0.07

S6 Comparing ΔMTh with the mean circulation part of the thermodynamic scaling

To examine the accuracy of the thermodynamic scaling in reproducing thermodynamic contributions to the moisture budget, we compare ΔMTh with a version of the thermodynamic scaling in which only the mean flow components are included (see Eq. 15 of the main manuscript). The results are shown in Fig. S4. Note, that we cannot directly evaluate the accuracy of the estimated thermodynamic contributions to submonthly eddy and interannual covariability driven $P - E$ changes, because these terms are not decomposed into thermodynamic, dynamic, and non-linear contributions in the moisture budget decomposition.
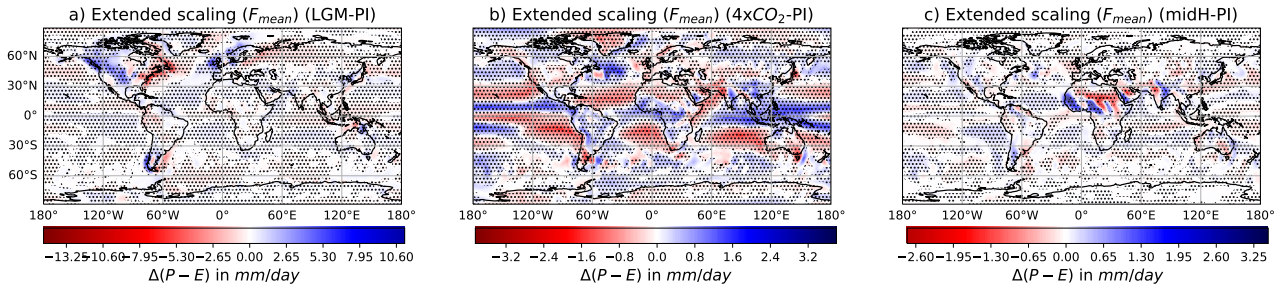

Figure S4: Annual mean extended thermodynamic scaling using only F_{mean} contributions (see Eq. 15 in the main manuscript) for (a) LGM, (b) 4xCO$_2$ and (c) midH. Stippling indicates sign agreement with ΔMTh.

S7 Statistical significance of WWDD / DWWD occurrence

Fig. S5 shows the results of the randomized experiments to test the statistical significance of the number of regions for which WWDD for 4xCO$_2$ or/and DWWD for LGM hold.
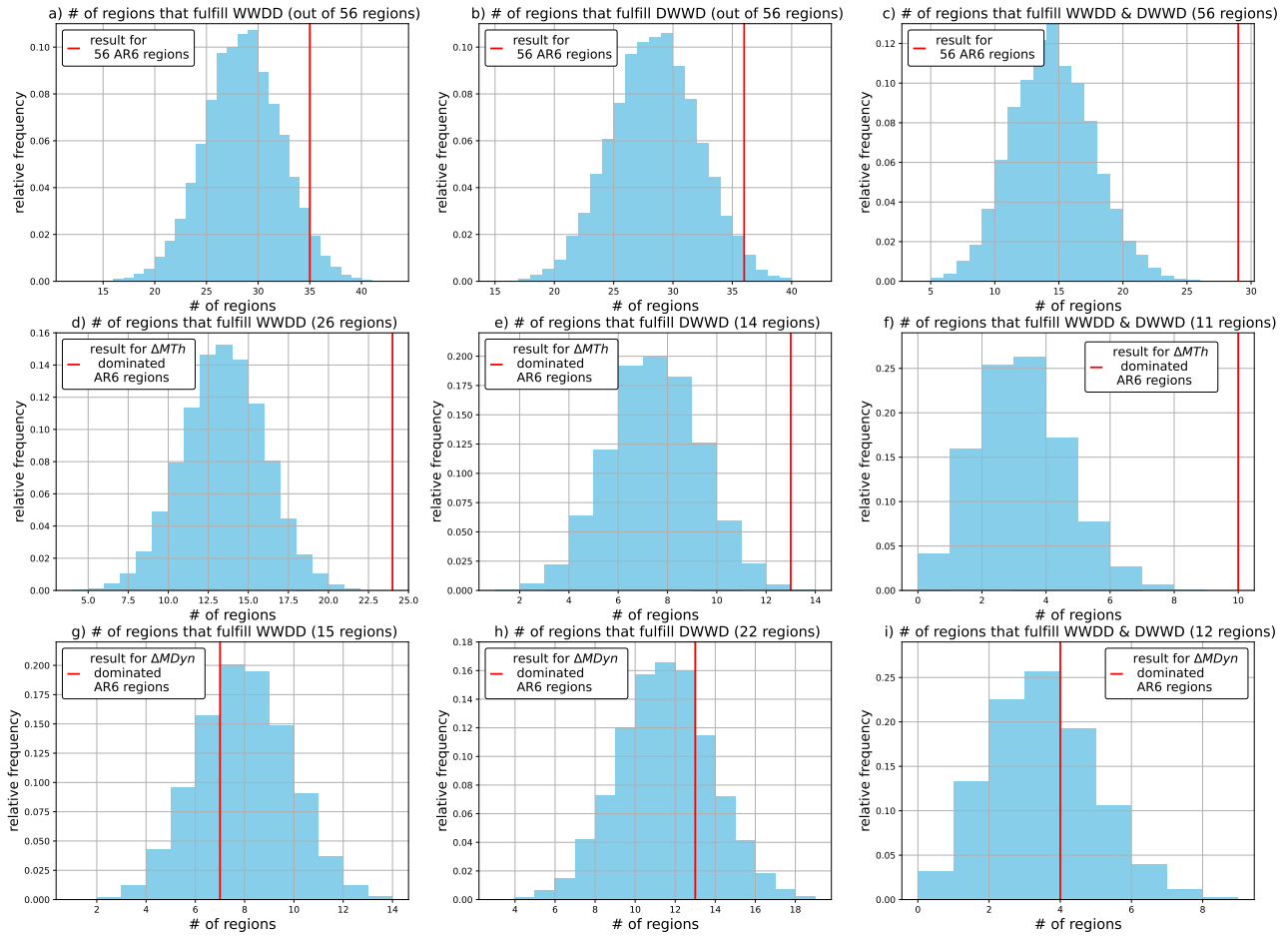
Figure S5: Results of the randomized experiments to test the statistical significance of the WWDD / DWWD occurrences, visualized as empirical probability distributions. Red lines indicate the number of regions that fulfilled the respective condition when directly comparing the PI, LGM and 4xCO$_2$ states.